Nano Research
2021, 14(4): 897–919

ISSN 1998-0124 CN 11-5974/O4
https://doi.org/10.1007/s12274-020-3018-z

Review Article

Recent advances in anisotropic two-dimensional materials and device applications

Jinlai Zhao[1,2,3,§], Dingtao Ma[2,§], Cong Wang[1], Zhinan Guo[1] (✉), Bin Zhang[1], Jianqing Li[2], Guohui Nie[1], Ni Xie[1] (✉), and Han Zhang[1] (✉)

[1] *Institute of Microscale Optoelectronics and Second People's Hospital, Health Science Center, Shenzhen University, Shenzhen 518060, China*
[2] *Faculty of Information Technology, Macau University of Science and Technology, Avenida Wai Long, Taipa, Macau 999078, China*
[3] *College of Materials Science and Engineering, Shenzhen Key Laboratory of Polymer Science and Technology, Guangdong Research Center for Interfacial Engineering of Functional Materials, Shenzhen 518060, China*
[§] *Jinlai Zhao and Dingtao Ma contributed equally to this work.*

Received: 11 May 2020 / **Revised:** 28 July 2020 / **Accepted:** 29 July 2020

ABSTRACT

Two-dimensional (2D) materials, such as transition metal dichalcogenides (TMDs), black phosphorus (BP), MXene and borophene, have aroused extensive attention since the discovery of graphene in 2004. They have wide range of applications in many research fields, such as optoelectronic devices, energy storage, catalysis, owing to their striking physical and chemical properties. Among them, anisotropic 2D material is one kind of 2D materials that possess different properties along different directions caused by the intrinsic anisotropic atoms' arrangement of the 2D materials, mainly including BP, borophene, low-symmetry TMDs ($ReSe_2$ and ReS_2) and group IV monochalcogenides (SnS, SnSe, GeS, and GeSe). Recently, a series of new devices has been fabricated based on these anisotropic 2D materials. In this review, we start from a brief introduction of the classifications, crystal structures, preparation techniques, stability, as well as the strategy to discriminate the anisotropic characteristics of 2D materials. Then, the recent advanced applications including electronic devices, optoelectronic devices, thermoelectric devices and nanomechanical devices based on the anisotropic 2D materials both in experiment and theory have been summarized. Finally, the current challenges and prospects in device designs, integration, mechanical analysis, and micro-/nano-fabrication techniques related to anisotropic 2D materials have been discussed. This review is aimed to give a generalized knowledge of anisotropic 2D materials and their current devices applications, and thus inspiring the exploration and development of other kinds of new anisotropic 2D materials and various novel device applications.

KEYWORDS

two-dimensional (2D) materials, low-symmetry, anisotropic properties, black phosphorus, device applications

1 Introduction

Two-dimensional (2D) materials, such as graphene, transition metal dichalcogenides (TMDs), and black phosphorus, have attracted extensive attention since the first discovery of graphene obtained through a simple scotch tape-based mechanical exfoliation method reported by Prof. Geim and his co-workers in 2004 [1]. Benefited from their excellent physical and chemical properties, 2D materials exhibit tremendous potential applications in many research areas, such as ultrafast lasers [2–7], optical switching and modulators [8–12], optoelectronic devices [13–26], thermoelectric devices [27–29], energy storage [30–36], catalysis [37–45], photothermal agents [46–51], cancer treatment and biosensing [52–58]. Compared with the bulk and traditional thin-film materials, 2D materials hold a great advantage and competitiveness for the device application. Take the photodetector applications on 2D materials as an example. Firstly, 2D layered materials with atomic thickness can provide very high transparency and excellent flexibility, which are very important and necessary for the integration of photovoltaic devices and wearable electronics. And the number of carriers in some 2D materials is much lower, which can effectively depress the dark current and achieve a high detectivity and on/off ratio. Secondly, the 2D quantum confinement effect in the vertical direction can lead to strong exciton binding effect, which can improve the optical absorption efficiency to a large extent [59]. For instance, the light absorption efficiency is around 2.3% per atomic layer thickness for monolayer grapheme [60]. Besides, the monolayer MoS_2 with a thickness less than 2 nm and direct bandgap, shows a light absorption efficiency estimated to be about 10% [59, 61, 62]. However, for anisotropic BP, the previous report demonstrated that the light absorption of BP nanosheet (with a thickness of 70 nm) is 40% and 10% along the armchair (AC) and zigzag (ZZ) direction, respectively [63]. Thirdly, most of the 2D materials possess a tunable bandgap with a direct relationship with the layer number. Therefore, the optical

Address correspondence to Zhinan Guo, guozhinan@szu.edu.cn; Ni Xie, xn100@szu.edu.cn; Han Zhang, hzhang@szu.edu.cn

absorption edge can be efficiently adjusted by regulating the layer number [59, 64]. Moreover, many kinds of 2D layered materials, graphene, TMDs, BP, borophene, to their different derivatives, can realize a wide photoresponse scope ranging from the extreme ultraviolet (10 to 100 nm) to long-wave infrared (12 to 30 μm) because of their various bandgaps [65]. Finally, 2D materials possess strong resistance to deformation capacity. And the stress between the 2D materials layers associated strongly with the electronic structure and optical properties [64]. In this case, stress engineering can be used to adjust their optical and electrical properties. In conclusions, those superior physical and chemical properties of 2D materials that beyond many bulk materials and other nanomaterials, would make the 2D materials becoming a research hotspot both in scientific study and technology development.

Comparing with some other similar reviews published before, the difference is listed as follows. Firstly, we focus on different types of anisotropic 2D material and then discussed their different anisotropic properties in separate chapters, respectively. More impressively, BP and borophene were highlighted as a most representative and newest anisotropic 2D materials in our review paper. Secondly, the method to identify the anisotropy of 2D materials were systematically summarized, such as, anisotropic conductivity, polarization-resolved infrared spectroscopy, angle-resolved polarized Raman spectroscopy, Young's modulus measurement by atomic force microscopy (AFM) nanoindentation, thermal conductivity test, especially for the novel method of anisotropic wetting of water droplets proposed by our group recently, which can be applied to identify the anisotropy of 2D materials quickly, accurately and nondestructively in a very low cost. Thirdly, the synthesis method, stability and the anisotropic properties of borophene are summarized fully and firstly in the anisotropic 2D materials field in our review paper. Finally, we summarized all different kinds of anisotropic properties for 2D materials in three tables, which include the different anisotropic performance along ZZ and AC direction and the anisotropic ratios. The readers can intuitively understand the difference in the anisotropy and device applications for different 2D materials.

1.1 Overview of typical anisotropic 2D materials

As an emerging star, anisotropic 2D materials with low-symmetry crystal structure, such as BP [66–72], rhenium disulfide (ReS_2) [73, 74], rhenium diselenide ($ReSe_2$) [75], group IV monochalcogenides (SnS, SnSe, GeS, and GeSe) [76–84], BP's alloy compound (B-AsP and GeP) and newly discovered borophene [85–87], are coming to us after the first reports of BP in 2014 from the groups of Zhang [88] and Ye [89, 90], which have been summarized in Fig. 1. As the firstly discovered anisotropic 2D material, puckered BP with orthorhombic structure in space group of *Cmca* has low-symmetry and the sp3 nonequivalent hybridization of each P atom, which result in a robust anisotropy nature in-plane in momentum space, including excellent anisotropic optical, electrical, thermal and mechanical properties [27, 68–71, 91–99]. Apart from BP, all of borophene, low-symmetry TMDs ($ReSe_2$ and ReS_2) and group IV monochalcogenides (SnS, SnSe, GeS, and GeSe) possess anisotropic crystal structures. For borophene, it possesses a honeycomb structure in the space group of *Pmmn*, which is similar with layered BP and leading to its high anisotropy. Besides, low-symmetry TMDs with orthorhombic (1Td WTe_2), monoclinic (1 T' $MoTe_2$) and triclinic (ReS_2 and $ReSe_2$) structures also have been proved to possess in-plane anisotropy due to the anisotropic crystal structure, which is different from the normal TMDs (MoS_2 and WSe_2) crystallizing in hexagonal phases. The anisotropy

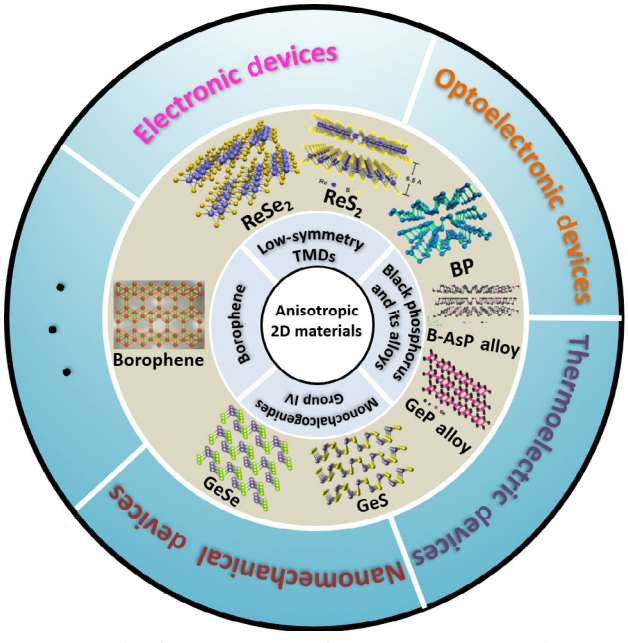

Figure 1 A brief summarization of anisotropic 2D materials, ranging from the classification, crystal structures, to the practical applications for different devices.

of Group IV monochalcogenides including two elements with different electronegativity comes from the similar puckered orthorhombic crystal structure as BP. Generally speaking, 2D materials with orthorhombic, monoclinic and triclinic crystal structures, namely low-symmetry crystal systems, will lead to in-plane anisotropic properties. These crystal structures may cause highly anisotropic physical properties, for example, electric conductivity and phonon group velocity. Meanwhile, the anisotropic physical properties promote extraordinary device applications that are impossible for isotropic materials [100]. The emerging anisotropic properties have motivated the innovation of electronic devices, optoelectronic devices, thermoelectric devices and nanomechanical devices based on these novel anisotropic 2D layered materials.

1.2 The method to identify the anisotropy of 2D materials

Considering the sufficient importance of anisotropic properties of 2D materials in the future research, especially in the device applications of electronic, optoelectronic, thermoelectric and nanomechanical devices, it is necessary and highly desirable to have a deep understanding of anisotropic properties of 2D materials and their detecting technology. Until now, many studies have been carried out both in experimental and theoretical aspects, and several effective techniques have been developed to identify the anisotropy for 2D materials. Here, as the most representative anisotropic 2D material, we take the BP as example to summarize the most popular and well acknowledged methods that have been applied for judging the anisotropy of 2D materials.

In order to independently determine the AC and ZZ direction of BP layers, Xia et al. [18] designed a field effect transistor (FET) that consists of 12 electrodes on the surface of BP layer spaced at an angle of 30° to study the angle-resolved direct current conductance, as shown in Figs. 2(a) and 2(b). Their measured results were fitted well with the calculated values. What's more, the results also revealed that the mobility in AC direction is about 1.5 times higher than that in the ZZ direction, demonstrating an obvious anisotropic mobility for

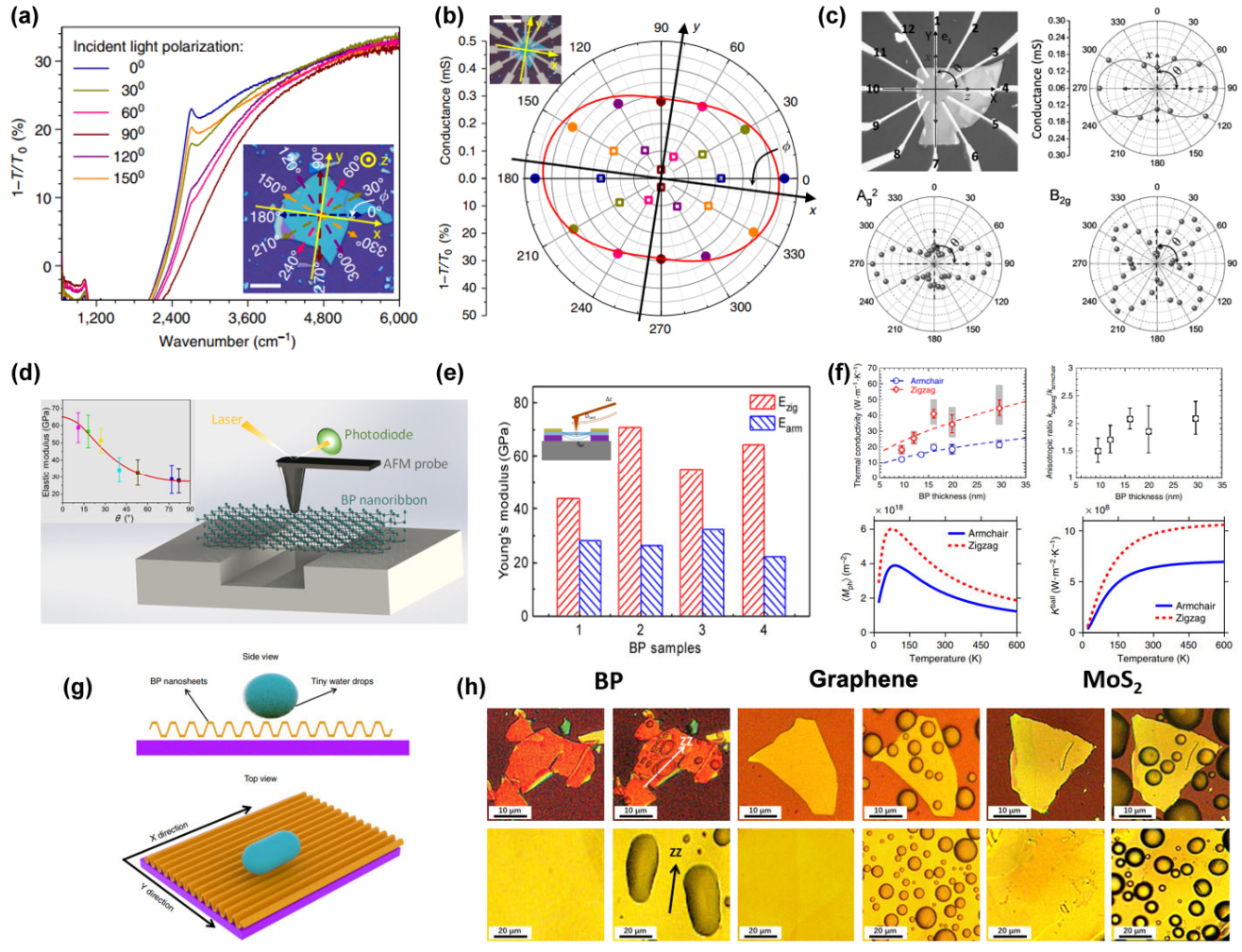

Figure 2 Different methods to identify the anisotropic properties of BP layers. Polarization-resolved infrared spectroscopy (a) and angle resolved DC conductivity (b) of BP thin film. The angle-resolved DC conductance (solid dots) and the polarization-resolved relative extinction of the same flake at 2,700 cm^{-1} (hollow squares) are shown on the same polar plot. In both (a) and (b), Φ is the angle between the *x*-direction and the 0 reference. (Reproduced with permission from Ref. [18], © Macmillan Publishers Limited 2014). (c) Identify the crystalline orientation of BP by using angle-resolved polarized Raman spectroscopy (ARPRS) method. (Reproduced with permission from Ref. [101], © WILEY-VCH Verlag GmbH & Co. KGaA, Weinheim 2015). (d) and (e) To distinguish the crystalline orientation of BP through anisotropic Young's Modulus along AC and ZZ direction by AFM. (Reproduced with permission from Ref. [102], © American Chemical Society 2015). (f) Anisotropic thermal conductivity of suspended BP layer both in. experiment (above) and theory (below). (Reproduced with permission from Refs. [93, 103], © Macmillan Publishers Limited 2015). (g) The schematic diagram of anisotropic wetting of water droplet on the surface of BP. The *x*-direction is in the ZZ structure and the *y*-direction is in the AC structure. (h) The anisotropic distribution of water droplets on BP layers and isotropic distribution of water droplets on 2D layered graphene and MoS_2. (Reproduced with permission from Ref. [104]. © Zhao, J. L. et al. 2019).

the BP. Unlike them, Wu et al. [101] employed an angle-resolved polarized Raman spectroscopy to detect the crystalline orientation of BP. As can be seen in Fig. 2(c), the Raman intensity of A_g^1, B_{2g}, and A_g^2 vibration modes in BP layer exhibited an obvious periodic change with the sample rotation angle under both cross and parallel polarization configurations, and the characteristic of those modes shows a huge difference. Based on the above results, they further demonstrated that A_g^2 mode can be applied to determine the specific crystalline orientation, because the relative smaller local maximum intensities of A_g^2 mode correspond to the ZZ direction of BP layer. On the other hand, Tao et al. [102] and Chen et al. [94] separately reported the anisotropic mechanical property of BP layer through suspended structures with the nanoindentation method by AFM, see in Figs. 2(d) and 2(e). The Young's modulus of few-layer BP were proved to be 58.6 ± 11.7 and 27.2 ± 4.1 GPa along the ZZ and AC directions, respectively. And the breaking stress were measured to be 4.79 ± 1.43 and 2.31 ± 0.71 GPa in the two directions. In addition, the ideal elastic modulus of BP nanoribbons along ZZ and AC direction are around 65 and 27 GPa, which were well consistent with the theoretical simulation results. In general, all the results indicated that highly anisotropic mechanical features are greatly expected to be helpful for the future applications of flexible electronics, nano-electromechanical systems, etc. Luo et al. [93] investigated the anisotropic in-plane thermal conductivity of suspended few-layer BP layers through the combination of experimental and theoretical methods, which combine the micro-Raman spectroscopy and first-principles calculations, as depicted in Fig. 2(f). The thermal conductivity anisotropic ratio of k_{ZZ}/k_{AC} was respectively calculated to be ~ 2 for thick BP layer (~ 15 nm) and ~ 1.5 for the thin layer (~ 9.5 nm), confirming a pronounced anisotropic thermal conductivity. Besides that, our group [104] recently put forward a unique approach both in experimental and theoretical [97] for fast (< 10 s) identification of the anisotropy of BP by the anisotropic wetting property of water droplets on the BP surface, see Figs. 2(g) and 2(h). Compared with the isotropic 2D materials, such as graphene and MoS_2, the water droplets condensed on the surface of BP from the water vapors are mainly elliptical, not spherical.

What's more, the long axis of the elliptical water droplets was along the ZZ direction of BP, which can be verified by the polarized-Raman spectroscopy. And this method has been proved to be non-destructive for layered BP through the *in-situ* Raman test and the electrical performance of BP-based FET after ten times repeated water wetting tests. This work can provide a significant guidance for the preparation and application of optical, optoelectronic, photothermal, thermoelectric and nano-mechanical devices that based on the anisotropic BP-like materials in the future.

2 The device applications based on typical anisotropic 2D materials

2.1 Anisotropic BP layers and its alloying compounds

2.1.1 *Synthesis and stability of BP*

In 1914, P. W. Bridgman [105] firstly discovered BP crystalline during an experiment that converted white phosphorus to red phosphorus under high hydrostatic pressure condition (200 °C, 1.2 GPa) within 5–30 min. In 1935, Hultgren et al. [106] adopted the X-ray diffraction (XRD) technique to confirm the orthorhombic crystal structure of BP and proved it a thermodynamically stable phosphorus allotrope [50]. In the 1980s, to improve the quality and size of BP single crystal, some Japanese groups made significant contributions to optimize the method to convert white phosphorus to BP [107–109]. Another mainstream method to synthesize BP crystalline is metal catalyst assisted growth [110] by the reaction of Hg, Au, Sn, red phosphorus, and SnI_4 in an evacuated silica ampule, at a relative low pressure and high temperature [111]. And this method was tremendously promoted by Nilges et al. in 2008 [112], and later was further simplified by Köpf et al. by using Sn/SnI_4 as the only mineralization additive [113]. Then in 2015, Li et al. [114] realized the large-area (up to 4 mm) synthesis of a nano-crystalline BP thin film (about 40 nm) through the direct conversion from red phosphorus thin films on flexible substrates under a high-pressure (beyond 8 GPa) multi anvil cell at room temperature (RT).

However, a principal challenge associated with BP is its environmental instability. Generally, the high surface area, hydrophilic phosphorus surface and reactivity of the exposed p-orbital lone paired electrons will make the BP layers susceptible to oxidize under the ambient conditions [115]. What's more, it has been recently demonstrated that the combination of light, oxygen and moisture would greatly accelerate the degradation of BP layers [116–119], and degrade the semiconducting properties. In order to protect it from being oxidized, many effective approaches have been developed, including covered with h-BN [120], atomic layer deposition of Al_2O_3 [116, 121], a double-layer comprising Al_2O_3 [122, 123], and a hydrophobic fluoropolymer. Among them, the former double-layer method appears to offer infinite stability by guaranteeing conformal sidewall coverage to prevent edge diffusion and moisture resistance from an effective hydrophobic surface. Notably, such strategies were further developed by our group. On one hand, Guo et al. [124, 125] reported a metal-ion modification (Ag^+, Fe^{3+}, Mg^{2+} and Hg^{2+}) to enhance both the stability and transistor performance of BP layers. Metal-ion spontaneously adsorbed on the surface of BP layers through cation–π interactions passivates the lone paired electrons of phosphorus atoms, and thereby making BP layers more stable in air. On this basis, we also demonstrated that the Ag^+-modified BP based FET exhibit a hole mobility of 1,666 $cm^2 \cdot V^{-1} \cdot s^{-1}$, which was around 2 times higher than that of bare BP. Besides, the ON/OFF ratio of Ag^+-modified BP based FET could reach 2.6×10^6, approximately 44 times higher than that of bare BP. On the other hand, Tang et al. [126] used a one-step, ionic liquid-assisted electrochemical exfoliation to fabricate fluorinated phosphorene (FP), and realize the improved stability of BP. The experimental and theoretical studies revealed that the enhanced air stability was mainly ascribed to the antihydration and antioxidation effects originated from the introduced fluorine adatoms.

2.1.2 *Anisotropic property of BP*

2.1.2.1 *Anisotropic electrical and photoelectric of layered BP*

For BP layers, the characteristics of high photoresponse [127–130] at mid-infrared wavelengths (3.39 μm) [131–133], large tunable bandgaps (0.3–1.8 eV) and unique polarization-dependent response can make it widely applied for the device applications, such as chip-scale mid-infrared sensing and imaging devices [133–140], optoelectronic devices [25, 68, 141–143], and thermoelectric devices [144].

In order to collect photo-generated carriers along both *x*-(AC) and *y*-(ZZ) direction, a BP-based photodetector device with four quadruple electrodes were fabricated, as shown in Fig. 3(c), and the thickness of the BP layer was around 12 nm. The drain bias of V_{DS} was fixed at 100 mV, then the relationship of sweeping gate voltage V_g, and source-drain current I_{DS} was measured, as shown in Fig. 3(d). An on-off current ratio of approximately 10^3 can be achieved, and the field-effect mobility along the *x*-direction (μ_x = 194 $cm^2 \cdot V^{-1} \cdot s^{-1}$) is about 1.6 times higher than that in the *y*-direction (μ_y = 122 $cm^2 \cdot V^{-1} \cdot s^{-1}$). The lower electron current should be attributed to a higher Schottky barrier, or conductive electrons being captured at the interface of BP/SiO_2. Figure 3(b) shows the results of photocurrent as a function of gate voltage at a fixed source-drain bias (V_{sd} = 200 mV) under 532 nm illumination (power = 230 μW) for a BP MSM photodetector operating at 3.39 μm (Fig. 3(a)). A different photocurrent peak can be obtained with the V_g sweeping from −0 to 20 V. The peak intensity in the *x*-direction is around 3 times larger than that in the *y*-direction, where *xx* and *yy* mean light polarization and carrier collection direction both along x- or y- direction. The higher carrier mobility and shorter carrier transit time along the *x*-direction attribute to another factor of 1.5–1.6 in terms of photocarrier collection.

A schematic illustration of photoelectric FET is shown in Figs. 3(e) and 3(f). The height profile presents the typical thickness of BP crystal used in the devices is about 4.5 nm. Firstly, Raman spectroscopy was applied (Fig. 3(g)) to determine the orientation of the crystal axis. The first-principle calculations result of Raman tensor indicated that the intensity of A^1_g and A^2_g modes is much lower along the ZZ direction (*y*) than that in the AC direction (*x*) for the BP. Besides, the ratio of Raman tensor between R_{xx} and R_{yy} is R_{xx}/R_{yy} = 140 and 300 for A^1_g and A^2_g mode, respectively. Therefore, from the intensity-dependent of the A^2_g mode on the polarization angle, it indicates that the source and drain (SD) direction is along the ZZ direction (*y*-axis) of BP crystal. Secondly, the change of photocurrent induced by the anisotropic BP crystal structure along with the variation of polarization angle is clearly depicted in Fig. 3(h). The intensity of photocurrent exhibits a rotational symmetry of 180, and minimizes at 0° and 180° while maximizes at 90° and 270°. However, since the electron hole pairs are separated and collected more efficiently when ZZ direction is parallel to the DC field, the shape of the curve is a little narrower along the AC direction.

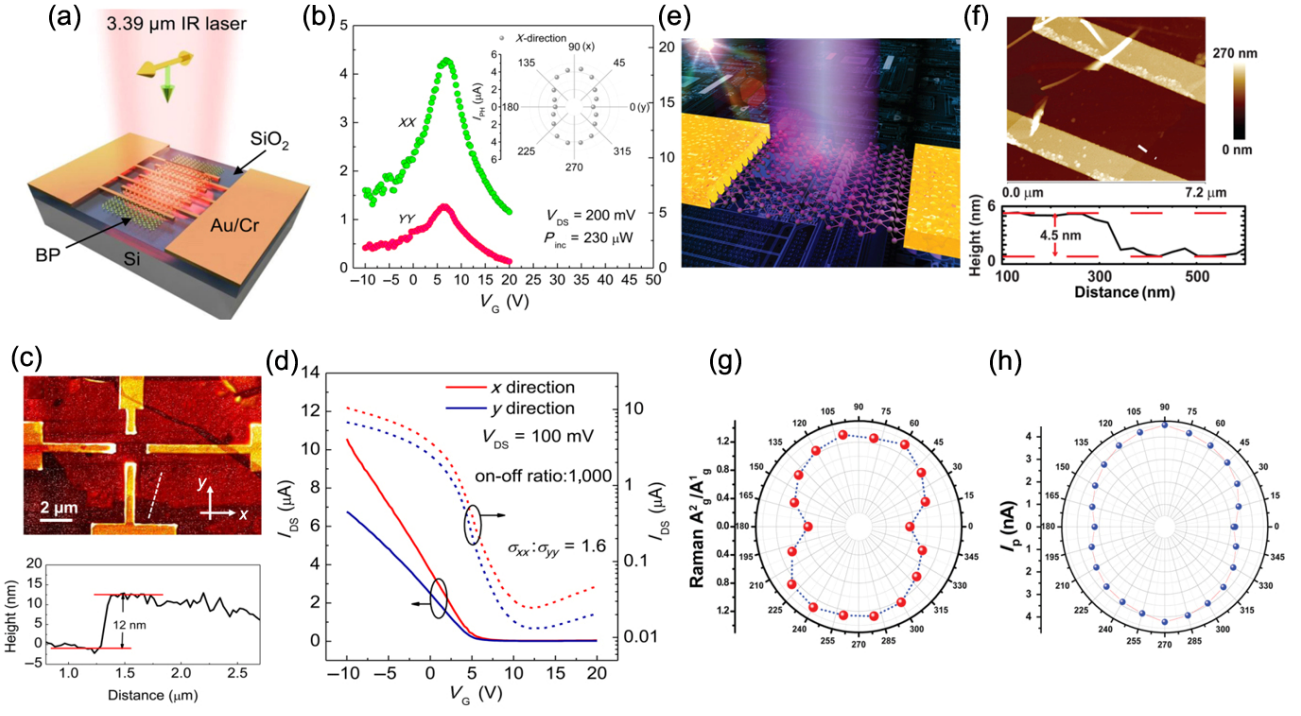

Figure 3 (a) Illustration of the BP MSM photodetector operating at 3.39 μm. (b) Effects of polarization, transport direction, and back gate voltage on the photocurrent generation/responsivity in the BP transistor. (c) Top: AFM image of the BP photodetector. The *x*- and *y*-directions are labeled in the image. Bottom: Height profile along the white dashed line in the top panel. (d) Transfer characteristics of the BP field-effect transistor. (Reproduced with permission from Ref. [141], © American Chemical Society 2016). (e) Three-dimensional view of the device structure used to measure photo response. (f) AFM scan across the channel area of our device showing the thickness of the BP flake to be ~ 4.5 nm. (g) Measured polarization dependence of the intensity of the A^2_g/A^1_g Raman peak. (h) Photocurrent measured with laser source of 405 nm wavelength at different light polarization angle. (Reproduced with permission from Ref. [145], © Chen, X. L. et al. 2017).

A ring-shaped metal electrode was designed as a photocurrent collector (Fig. 4(a)) to observe 2 times polarization-dependent photocurrent from a geometric edge effect at the metal-BP edge. And the photogenerated hot carriers from the ring-shaped metal electrode can be collected isotopically. Compared with the conventional phototransistors, the photogenerated electrons and holes from the vertical p-n junction can be easily separated by selectively driving them into surface or bulk layers under a built-in electric field in the electric-double-layer transistor (EDLT). Therefore, this vertical p-n junction structure can greatly improve the efficiency of linear dichroism photodetectors. Figure 4(b) shows a full spatial mapping of the photocurrent around the ring-shaped electrode under 1,500 nm illumination. Focusing the excitation in the round area within the inner diameter of the electrode, the photocurrent with 0° light polarization is much larger than that for 90° light polarization, suggesting that the intrinsic polarization-dependent photo response originates from the BP itself. The photo-responsivity is about 0.35 mA·W^{-1} at 1,200 nm, and there is a relatively large contrast ratio (3.5) between the photo-responsivities along the two perpendicular polarizations. Figure 4(d) clearly indicates that the incident light at different polarization states will experience a varying absorption when travelling through the dichroic BP, directly reflecting the intrinsically anisotropic orientation of the crystal structure.

As shown in Fig. 5(a), dual-gate h-BN/BP/h-BN-based FET was fabricated by using a polymer-free dry transfer method, BP film was sandwiched by h-BN flakes and transferred onto a silicon substrate covered with a 90 nm-thick silicon dioxide. The cross-sectional high-resolution transmission electron microscopy (HRTEM) image demonstrated the clean and oxidation-free BP/h-BN interfaces, which can be further evidenced by the elemental mapping for nitrogen (blue), phosphorus (green), and oxygen (red), as shown in the right panel of Fig. 5(b), and no oxygen signal was observed within the h-BN/BP/h-BN heterostructure. In that device, the BP thin film was 10-layers thickness and the h-BN layers on the top and bottom were 23 and 9 nm-thickness, respectively. The top h-BN dielectric consisted of two h-BN layers transferred separately. One is used to sandwich the BP film, while the other was transferred after the deposition of the interdigitated chromium/gold (3/27 nm) fingers for photocurrent collection, and covering the channel and the electrodes. These interdigitated electrodes were designed along the *y*-direction (ZZ) of BP thin flakes so that the carrier can be collected along the *x*-direction (AC), in order to achieve the highest carrier mobility and photo-responsivity. The BP crystalline direction was identified by the polarization-resolved Raman spectroscopy, in which the intensity ratio of peaks A_g^2 and A_g^1 reaches a maximum value of 3.8 when the polarization of excitation laser was aligned along the *X*-direction, as shown in Fig. 5(c). The photo-response of BP thin films also shows the strong angle dependence at all three representative mid-IR wavelengths. Figure 5(d) shows the photo-response at 5 μm with light polarization at different angles as an example. The responsivity can reach the maximum value when the light polarization was along the *x*-direction (AC), while achieving the minimum value along the *y*-direction. Such phenomenon can be attributed to the small optical absorption coefficient along the *y*-direction of BP owing to its unique puckered lattice structure.

The authors revealed the highly anisotropic and strongly bound excitons in monolayer BP using polarization-resolved photoluminescence measurements at RT. And regardless of the excitation laser polarization, the results showed that the emitted light from the monolayer is linearly polarized along the light effective mass direction and centered around 1.3 eV,

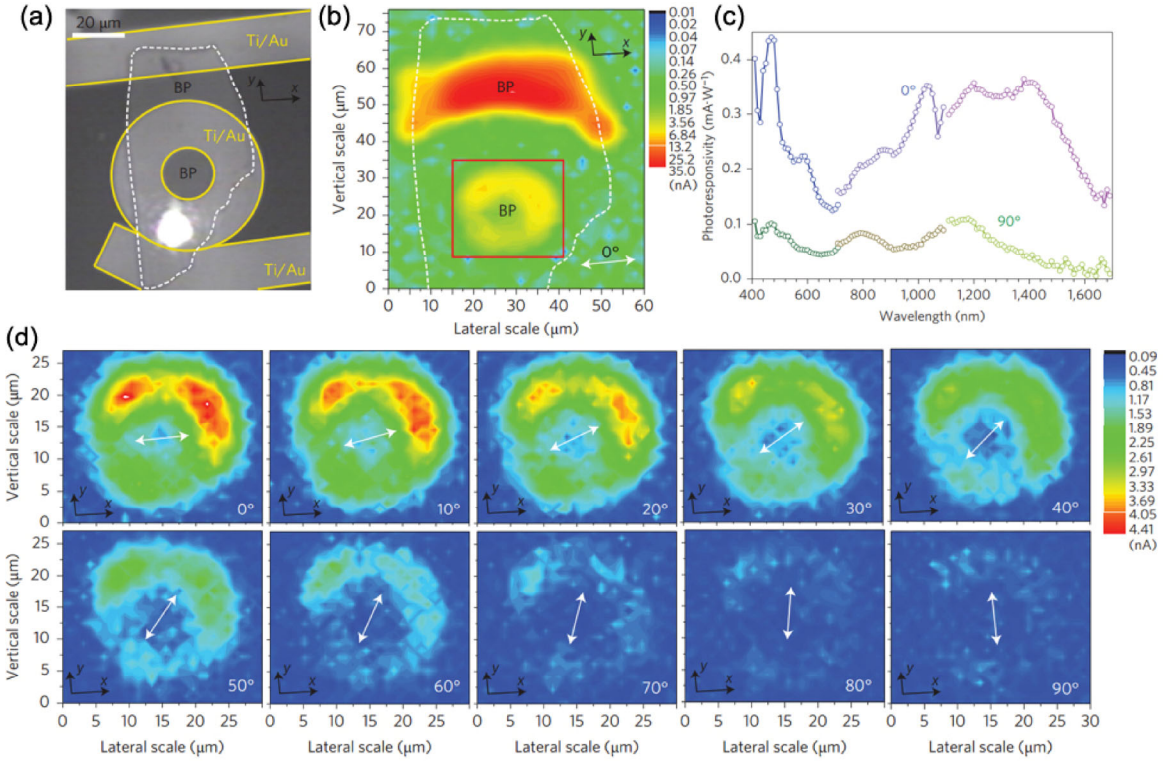

Figure 4 (a) Optical image of a BP photodetector with a ring-shaped photocurrent collector. (b) Corresponding photocurrent microscopy image of the device shown in (a). (c) Polarization dependence of photoresponsivity with illumination from 400 to 1,700 nm, where the polarization angle of 0° corresponds to the *x* crystal axis and 90° corresponds to the *y* crystal axis. (d) Photocurrent microscopy images of the BP inside the inner ring under illumination at 1,500 nm with different light polarizations (white arrows). (Reproduced with permission from Ref. [146], © Macmillan Publishers Limited 2015).

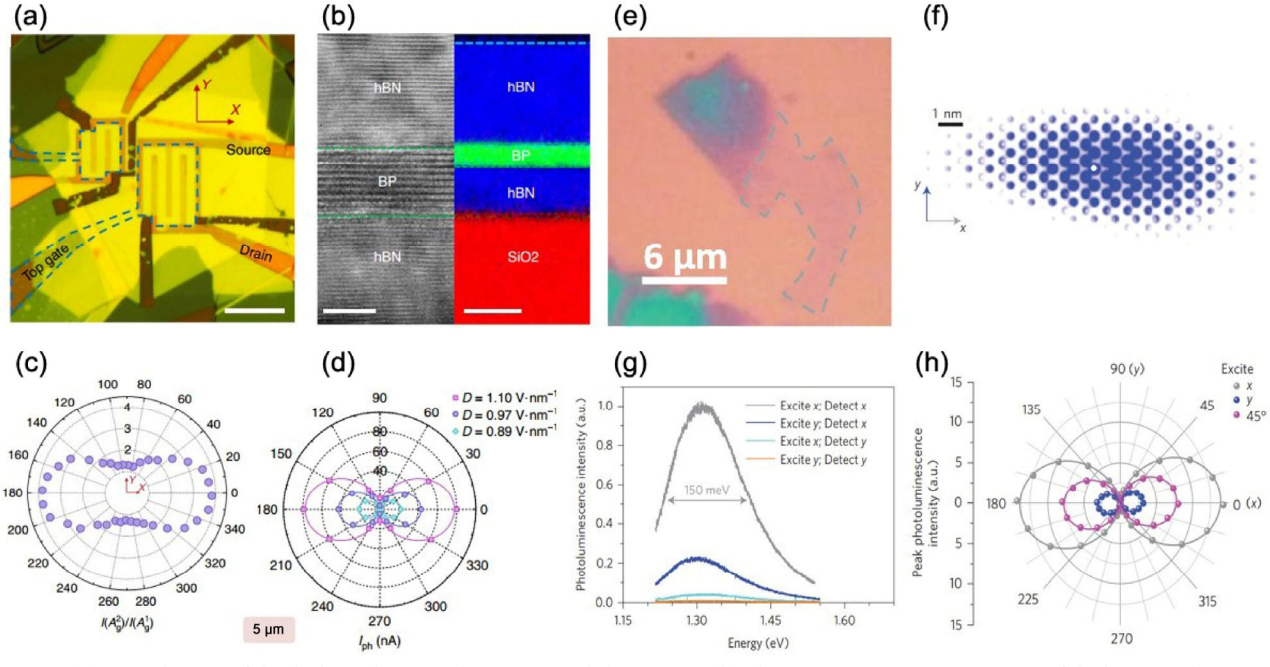

Figure 5 (a) Optical image of the dual-gate h-BN/BP/h-BN FET, scale bar: 10 μm. (b) The cross-section HR-TEM image of the h-BN/BP/h-BN stack. (c) The ratio of Raman A_g^2 and A_g^1 peak intensity as a function of the excitation laser polarization. (d) Scatters show the photocurrent at different laser polarizations for the 5 μm incident laser. (e) Optical micrograph of an exfoliated monolayer black phosphorus flake on 285 nm SiO_2 on a silicon substrate. The monolayer region is indicated by the grey dashed line. (f) Polarization resolved Raman scattering spectra of monolayer BP with linearly polarized laser excitation. (g) Polarization-resolved photoluminescence spectra for monolayer BP. (h) Photoluminescence peak intensity as a function of polarization detection angle for excitation laser polarized along *x* (grey), 45°(magenta) and *y* (blue) directions. (Reproduced with permission from Ref. [71], © Macmillan Publishers Limited 2015).

which was a clear signature of emission from highly anisotropic bright excitons. Moreover, photoluminescence excitation spectroscopy suggested a quasiparticle bandgap of 2.2 eV, from which we can estimate an exciton binding energy of ~ 0.9 eV, and be consistent with the theoretical results based on first principles calculation. Excitation polarization and detection were selectively oriented along either the *x* or *y* axes, giving a total of four different spectra. Regardless of the excitation or

detection polarization, the emission spectrum showed a single peak with a full-width at half-maximum (FWHM) of ~ 150 meV and centered at ~ 1.3 eV. And the highest photoluminescence intensity occurred when both excitation and detection polarizations were aligned with the *x*-direction, as showed in Fig. 5(g). Figure 5(f) depicts the electron wavefunction of the bright ground-state exciton of monolayer BP based on first-principles GW–Bethe–Salpeter equation theory. Since the wavefunction is strongly extended along the *x*-direction, the observation of highly polarized emission indicates the excitonic nature of the observed photoluminescence. The carriers are more mobile in the dispersive band along the *x*-direction than in the flat band along the *y*-direction, and the isotropic Coulomb interaction thus binds the carriers most strongly in the *y*-direction. Figure 5(h) shows that the photoluminescence always originated from these anisotropic excitons, the emitted light was strongly polarized along the *x*-direction, regardless of the excitation polarization. And these results represent the first experimental demonstration of anisotropic excitons in 2D materials.

2.1.2.2 *Anisotropic in-plane thermoelectric of layered BP*

Expect outstanding anisotropic electronic, optical and optoelectronic properties mentioned above, the in-plane anisotropic thermal transport in BP layers is also believed to be an intrinsic property, which can be induced by anisotropic phonon dispersion and phonon-phonon scattering rate along the AC and ZZ directions. Lately, the thermoelectric performance of bulk BP has been studied in experiment, which indicated that BP nanosheets could be applied as an efficient thermoelectric material [144]. And many other works have already predicted that monolayer and few layers BP possess very distinct anisotropic in-plane thermal transport in theory. Theories speculate that BP layers behave completely opposite anisotropic properties in thermal and electrical conductivities. That's to say, there is a higher electrical conductivity along the AC direction, while higher thermal conductivity along the ZZ direction for BP layers [27, 93, 103, 147–150].

Fei et al. [27] adopted first-principles and model calculations methods to prove that monolayer BP not only has a spatially anisotropic electrical conductance, but also has pronounced spatial-anisotropy lattice thermal conductance, as shown in Fig. 6(a). The thermal conductance was always larger along the ZZ direction than that in the AC direction when the temperature ranging from 200 to 400 K. In addition, the preferred direction for thermal conductance in monolayer BP lies perpendicular to that of electrical conductance, as depicted in Figs. 6(a) and 6(b), which is consistent with the theoretical calculation results mentioned above. Lately, Lee et al. [103] proved in experiment that BP nanoribbons possess a higher *k* along the ZZ direction than that in the AC direction, by as much as 7 $W \cdot m^{-1} \cdot K^{-1}$ at temperatures above 100 K, however, both directions have similar *k* at lower temperatures ranging from 30 to100 K, as revealed in Fig. 6(c). The anisotropy ratio k, which means the ratio along the ZZ and AC directions, increases with temperature rising, and it can reach up to 2 at 300 K. The reason is that the phonon-phonon scattering will become the dominating scattering with the increasing temperature, which leads to the increasing anisotropy ratio. In 2015, Luo et al. [93] demonstrated that the thermal conductivities of AC and ZZ directions are respectively about 20 and 40 $W \cdot m^{-1} \cdot K^{-1}$ for BP layers when the thickness is greater than 15 nm, while as the thickness reduces, the thermal conductivities will decrease to about 10 and 20 $W \cdot m^{-1} \cdot K^{-1}$, measured by micro-Raman spectroscopy and shown in Fig. 6(d). Meanwhile, the anisotropic ratio of thermal conductance was proved to be about 2 for thick BP layers, and decreases to about 1.5 for the thinnest BP layer (9.5 nm) (see in Fig. 6(e)).

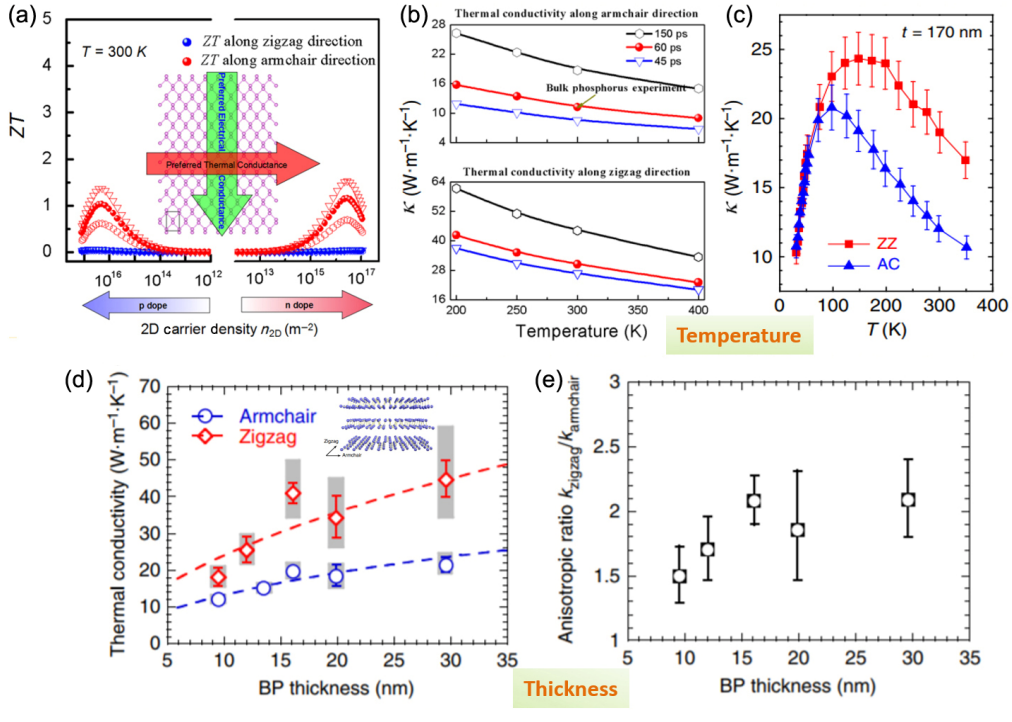

Figure 6 Anisotropic in-plane thermoelectric of layered BP. (a) The calculated value of ZT in monolayer BP along *x*- and y-directions at 300 K. (b) Thermal conductance of monolayer phosphorene along the AC and ZZ directions, respectively. (Reproduced with permission from Ref. [27], © American Chemical Society 2014). (c) Thermal conductivity versus temperature plot of BP nanoribbons axially oriented to the ZZ and AC directions, respectively. (Reproduced with permission from Ref. [103], © Macmillan Publishers Limited 2015). (d) Extracted AC and ZZ in-plane thermal conductivities (k_{AC} and k_{ZZ}) of multiple BP layers in theory. (e) The anisotropic ratio k_{ZZ}/k_{AC} at different thicknesses of BP layers by calculation. (Reproduced with permission from Ref. [93]. © Macmillan Publishers Limited 2015).

2.1.2.3 *Anisotropic mechanical properties of layered BP*

Comparing with some other anisotropic properties of layered BP, such as electric, photoelectric, and thermoelectric properties, anisotropic nanomechanical property is more intriguing and crucial but remain less well investigated. As we all know that the mechanical properties of 2D nanomaterials are very important for various novel applications, such as flexible and wearable electronics, electro-mechanical resonators, strain sensors and even nanoscale generators [152–159] in the future. Meanwhile, the mechanical properties of 2D materials reveal plentiful physics and provide valuable insights into the lattice electron interactions in 2D materials systems. Recent research demonstrated that the strain of BP layer can affect the electrical properties remarkably. So, it is very necessary to take consideration of the mechanical anisotropy when design and fabricate nanoelectronic and photoelectric devices based on BP layers. These unique anisotropic mechanical properties are very valuable and meaningful for both scientific studies and exploration of peculiar mechanical and electronic applications.

As early as 2014, Jiang et al. [155] adopted first-principles calculations to study the mechanical properties of single-layer BP under uniaxial deformation. The effective Young's modulus of single-layer BP was proved to be 21.9 $N \cdot m^{-1}$ along the AC direction and 56.3 $N \cdot m^{-1}$ along the ZZ direction with a ratio of approximately 2.5, which is very rare among 2D and bulk materials for such large anisotropy ratio. In 2015, Tao et al. [102] studied the anisotropic mechanical properties of few-layer BP by using an nanoindention system based on AFM. The results revealed that the strength of BP is highly anisotropic. As shown in Fig. 7(b), the Young's modulus of few-layer BP was 58.6 ± 11.7 and 27.2 ± 4.1 GPa along the ZZ and AC directions, respectively, while their corresponding breaking stress was 4.79 ± 1.43 and 2.31 ± 0.71 GPa (Fig. 7(c)). Lately, Chen et al. [94] investigated the mechanical properties of suspended BP nanoribbons on narrow grooves by AFM system and the strongly anisotropic mechanical properties of BP nanoribbons were perfectly proved by the experiments. The elastic modulus of the suspended BP nanoribbons along the ZZ direction (65 GPa) was the largest and almost 2.4 times larger than that along the AC direction (27 GPa), which agrees well with the simulation results obtained by theoretical calculations (Fig. 7(a)). Wang et al. [151] studied the effects of mechanical anisotropy on multimode responses in BP nanoresonators by using the method of finite element modeling (FEM). From the multimode resonant responses (Figs. 7(d) and 7(e)), the authors determined the elastic modulus to be E_{Yy} = 116.1 GPa (ZZ direction) and E_{Yx} = 46.5 GPa (AC direction) in the BP crystal, as shown in Fig. 7(f), which manifested the unique mechanical anisotropy effects well in BP nanodevices.

2.1.3 *Anisotropic property of BP alloying compound*

Alloying is one of the general strategies that has been applied for tuning the performances of materials for thousands of years [160]. And graphene, h-BN, and TMDs with tunable performances can be synthesized through such alloying methods [161–164]. So, through the combination of phosphorus (P) element with the Group IV elements, such as C, Si, Ge, As, Sn, Te, it can be greatly expected to come into being materials with integrating advantages for both groups, for instance, good chemical, physical, thermal [160] and dynamic stability, high mobility, moderate adjustable band gap and in-plane or out of plane anisotropy [75, 160, 165–169]. Therefore, group IV-P compound materials with kinds of anisotropic properties possess promising future for both electronic and optoelectronic applications [170].

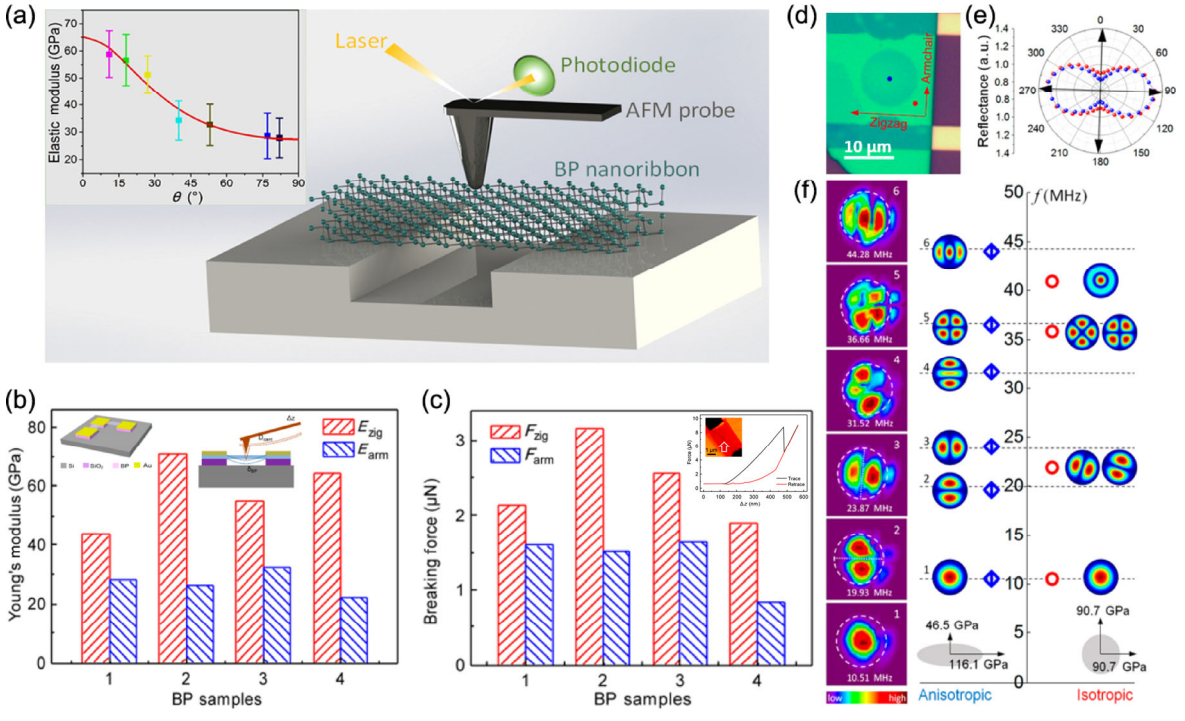

Figure 7 Anisotropic mechanical properties of layered BP. (a) Elastic modulus of BP nanoribbons suspended on narrow grooves versus different included angles and testing schematic by AFM indention. (Reproduced with permission from Ref. [94]. © American Chemical Society 2016). ((b) and (c)) The anisotropic Young's modulus and breaking force for few-layer BP. (Reproduced with permission from Ref. [102], © American Chemical Society 2015). (d) Optical image showing the crystal directions determined from the multimode resonance measurement. (e) Polarized optical reflectance measurement of the same flake using 532 nm illumination. The blue and red data are measured at the locations indicated by the blue and red dots in (d). (f) left column-measured multimode resonance of a circular BP mechanical resonator. Middle column-simulated anisotropic resonator. Right column-simulated isotropic resonator. (Reproduced with permission from Ref. [151], © American Chemical Society 2016).

In 1994, Shirotani et al. proved that arsenic can be incorporated into BP to form black arsenic-phosphorus (b-AsP) alloys via a high pressure and high temperatures process, and such compound material showed a good superconducting properties at about 10 K [171]. Recently, Liu et al. [160] demonstrated a new synthetic method by adopting the alloying strategy to prepare layered b-AsP with different and tunable compositions (b-As_xP_{1-x}, x = 0–0.83). Owing to the good tunability of the chemical compositions, layered b-AsP materials possess fully tunable bandgaps down to about 0.15 eV, which is only half of the bandgap of monolayer BP (around 0.3 eV) and reaches the long wave infrared (LWIR) regime [160, 167]. In 2016, Barreteau et al. [172] grew SiP and GeP bulk single crystals from the melt in a high-pressure (0.5–1 GPa) cubic anvil hot press. Polycrystalline SiP has also been successfully synthesized via a chemical vapor transport (CVT) strategy with the presence of I_2 as transport agent. Last year, Li et al. [168] fabricated 2D single crystals GeP with a mixture of Ge ingot, P powder, and Bi chunks in a tube under 950 °C for 24 h. And the angle-resolved electronic and optoelectronic measurements manifest that 2D GeP possesses the strong in-plane anisotropic conductance and photoresponsivity both in experimental and theoretical aspects.

Similar to BP, the layered b-AsP materials have orthorhombic crystal structure with a puckered honeycomb lattice. As and P atoms are distributed in the compound and the content of the unit cell ranges depends on the volume of As. Similar with other 2D layered materials such as graphene, BP, and TMDs, b-AsP materials possess strong in-plane covalent bonds as well as weak van der Walls interaction within interlayer. One major intention to study layered b-AsP is that it can be used to regulate the bandgaps by tuning the chemical compositions in the system. It demonstrated that the bandgaps of layered b-As_xP_{1-x} decrease with the increasing content of arsenic in the compound. What's more, the bandgaps of layered b-As_xP_{1-x} materials could be fully tuned ranging from 0.3 to 0.15 eV, which are even much smaller than that of monolayer BP. Importantly, photodetectors based on layered b-AsP showed a decent photo-response at mid-IR wavelength up to 8.2 μm [145, 173]. Polarization resolved infrared absorption spectroscopy and polarization-resolved micro-Raman spectroscopic studies revealed the in-plane anisotropic behavior of b-AsP. And the maximum absorption was found along the AC direction of b-AsP, while the polar maps of the intensity of Raman peaks corresponding to A_g^1, B_{2g}, and A_g^1 modes show the clear polarization-dependent Raman intensities like the layered BP.

GeP has the layered structure with an indirect band gap ranging from 0.51 eV for bulk state to 1.68 eV for monolayer, and its crystal structure is shown in Figs. 8(a) and 8(b). Typically, 2D layered GeP shows strong anisotropy of phonon vibrational conductance and photoresponsivity. Figure 8(c) shows the typical output curves along x- and y-directions under illumination, the device possesses a higher conductivity along the y-direction, exhibiting an obvious anisotropy. In addition, the anisotropic properties of conductivity is in good accordance with the calculated results of few-layer GeP reported previously [168]. The time-resolved photo-response exhibits both lower on and off current along x-direction than y-direction in Fig. 8(d). The angle-dependent dark conductivity of electrodes along the y-direction was defined as the 0° reference shown in Fig. 8(f). And the extracted anisotropic factor σ_y/σ_x (1.52) is comparable to the previously reported layered BP [141]. The angle-dependent photocurrent is also shown in Fig. 8(g). The I_{phy}/I_{phx} (1.83) was larger than anisotropic factor of dark conductivity σ_y/σ_x. This difference in the anisotropy factor between dark conductivity and photocurrent might be attributed to the anisotropic optical absorption of GeP, which has a higher absorption in the y-direction than that in the x-direction.

2.2 Anisotropic borophene

Boron element is located at the middle of beryllium and carbon in the periodic table of elements [174, 175], possessing vital chemical features of both nonmetal and metal. Due to the electron-deficient characteristic, many kinds of bonding way can be formed during the boron atoms, ranging from normal two-center-two-electron bonding to multicenter two-electron bonding, thus leading to the rich allotropes' structures.

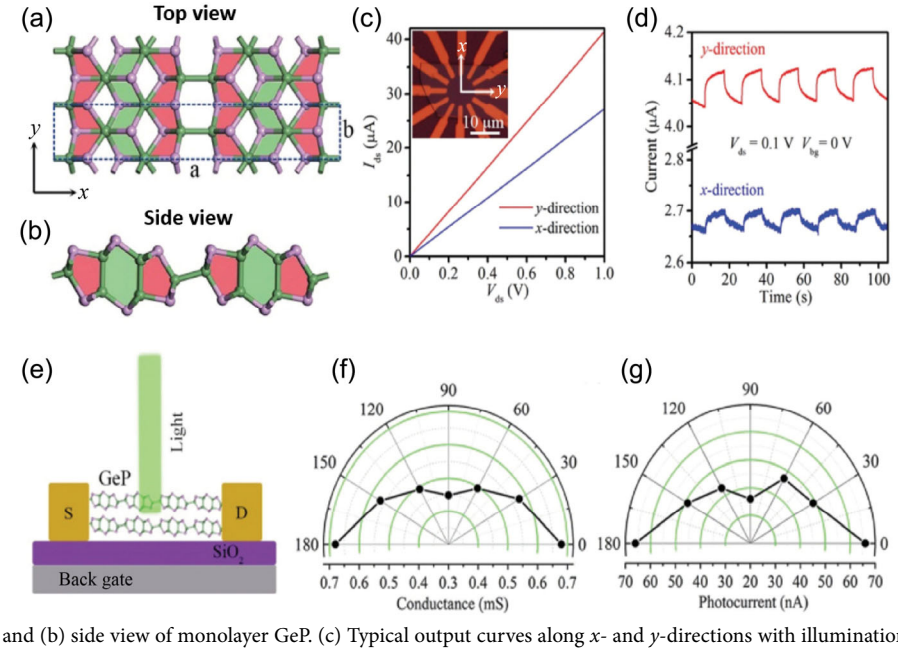

Figure 8 (a) Top view and (b) side view of monolayer GeP. (c) Typical output curves along x- and y-directions with illumination, inset: OM image of the device with x- and y-directions are labeled. (d) Time-resolved photo-response along x- and y-directions recorded at V_g = 0 V and V_{ds} = 0.1 V. (e) Schematic representation of the GeP FET. Angle-dependent conductance (f) photocurrent (g). (Reproduced with permission from Ref. [168], © WILEY-VCH Verlag GmbH & Co. KGaA, Weinheim 2018).

Until now, at least 16 kinds of boron allotropes with abundant promising properties have been reported [87, 174, 176–178]. Similar with carbon, boron possesses a short covalent radius and flexibility to adopt sp^2 hybridization, which would favor the formation of many low-dimensional allotropes, such as boron fullerenes, nanotubes and 2D boron sheets [174]. Recently, 2D monolayer of boron atoms, namely borophene, was successfully prepared in experiment and was shown to exhibit polymorphism [87, 174]. After that, borophene has attracted a plenty of research interest. In particular, the studies of density functional theory (DFT) and first-principles calculations have predicted the structure of borophene a metallic nature, despite the semiconductive nature of its bulk state [86, 176, 177, 179, 180]. Stable boron sheets with the hexagonal vacancy density (η) between and including 0 and 1/9 are buckled in theory. For those $1/9 \leq \eta \leq 1/5$ are flat, while those for $\eta \geq 1/5$, are unstable [181]. Among all the predicted boron sheets, the synthesis of δ_6 (η = 0), β_{12} (η = 1/6), and χ^3 (η = 1/5) have recently been reported in experiment [87, 174, 182]. The atomic structure of boron shows that the B atoms form line chains along the *x*-direction, however, the bonding between B atoms in different chains result in corrugation along the *y*-direction. Therefore, borophene possesses a high anisotropy with a honeycomb structure like layered BP in space group of *Pmmn*. As a comparison, the B atoms in the bottom and top layers are labeled as green and blue balls in Figs. 9(a) and 9(b), and band marked as B_1 and B_2, respectively.

2.2.1 *Synthesis and stability of borophene*

Comparing with other 2D materials which are stacked layer by layer in the bulk forms, such as graphene, h-BN, TMDs and BP, 2D boron has a very high energy than that of all its bulk forms. The thermodynamic instability of 2D boron and its intrinsic polymorphism lead to a really significant challenge for its synthesis [183]. In general, the most representative methods for synthesizing the ultrathin 2D boron nanosheets can be divided into the down-top and top-down strategies. For down-top method, the 2D boron sheets with single-atom thickness or ultrathin boron films can be grown and prepared on a substrate, such as Ag (111) [174, 184, 185], Cu (111) [182, 186] and Au (111) [187, 188] under ultrahigh vacuum (UHV) conditions through molecular beam epitaxy (MBE), CVD and templated growth method.

In early 2015, for the first time, Mannix et al. [87] successfully fabricated the borophene (δ_6) under UHV conditions by using a solid B atomic source on the substrate of Ag (111) through MBE, like Figs. 9(a) and 9(d) show. And they also demonstrated that borophene exhibits metallic properties that are consistent with predictions of a highly anisotropic. Two years later, Wu et al. [182] reported that large-area (up to 100 μm^2 in size) single-crystal thin films of borophene on Cu (111) surface in an ultrahigh-vacuum low energy electron microscopy (LEEM) system augmented with MBE capability. During the growth of borophene, it can monitor progress of real-time of dynamics of borophene nucleation and growth and *k*-space structural characterization simultaneously by the system of low energy electron diffraction (LEED). The crystal structure of borophene was demonstrated to be a new triangular network with a density of hexagonal vacancies of η = 1/5 (χ^3) by a high-resolution scanning tunneling microscopy (HRSTM). Unlike previous studies that grow borophene on the substrates of Ag (111) and Cu (111) by MBE and CVD methods, recently,

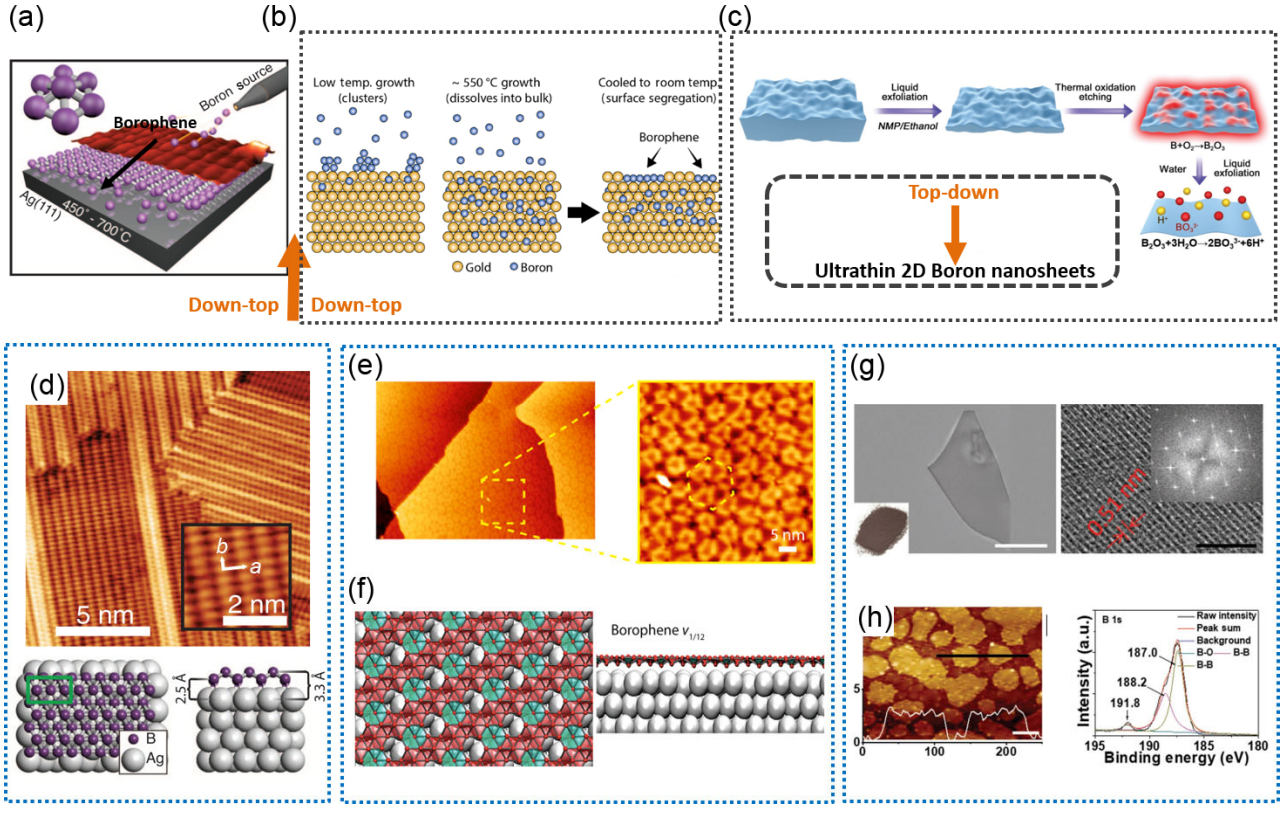

Figure 9 Two main methods to prepare borophene down-top method ((a) and (b)) and top-down method (c). (d) STM topography image of borophene and computational prediction of borophene structure with low-energy (Reproduced with permission from Ref. [184], © American Association for the Advancement of Science 2015). (e) STM image of trigonal network Borophene on Au (111) surface. (f) Atomic structure of the borophene $v_{1/12}$ computationally modeled and predicted for Au (111) (left, top down view; right, cross-sectional view). (Reproduced with permission from Ref. [187], © American Chemical Society 2019). (g) TEM and HRTEM image (inset: FFT diffraction patterns) of liquid exfoliated B NSs. (h) AFM image and XPS spectra of liquid exfoliated B NSs. (Reproduced with permission from Ref. [189], © WILEY-VCH Verlag GmbH & Co. KGaA, Weinheim 2018).

Kiraly et al. [187] proposed a templated growth method to prepare borophene. The boron atoms firstly diffuse into Au (111) at high temperatures, and then segregate to the Au (111) surface to form borophene with metallic electronic structures as the substrate is cooled, as shown in Fig. 9(b). The growth mechanism is that Au (111) surface with few low-energy undergoes a rebuild to minimize surface energy, which leads to nanoscale templating of borophene nucleation and growth, like Figs. 9(e) and 9(f) show.

On the other hand, the top-down methods, including chemical exfoliation (CE), and sonication-assisted liquid-phase exfoliation (LPE) [190, 191] also have been demonstrated to be efficient for the preparation of 2D boron sheets. Unlike any other 2D materials with layered structures naturally, boron exhibits more complex and diverse bulk structures due to rich bonding structures among boron atoms, thus making it difficult to fabricate ultrathin boron nanosheets (B NSs) through direct exfoliation. In 2018, Ji et al. [189] prepared high-quality ultrathin B NSs in large quantities (Fig. 9(c)) by coupling liquid exfoliation and thermal oxidation etching technologies, with the controllable thickness in nanoscale size (about 100 nm of planar size and below 5 nm of thickness, see in Figs. 9(g) and 9(h)). The fundamental mechanism of this approach is that the B–B units from the thick B layers can be easily oxidized in air at a high temperature (600–700 °C) to form B_2O_3, which can be dissolved into water to form BO_3^{3-} by probe sonication.The as-prepared B NSs can be evaluated as a novel and superior photothermal agents (PTAs) for cancer photothermal therapy (PTT) and photothermal and photoacoustic (PA) imaging after being modified by polyethylene glycol (PEG-NH_2) via electrostatic adsorption.

In a word, 2D B nanosheets, even borophene, can be prepared successfully by both top-down and down-top methods, however, the exact crystal structure of 2D B is still disputed. More importantly, the nanometer size single-crystal layers prepared so far are too small to apply for the device. Another critical challenge is the transfer of borophene from the metal substrate (Au, Ag, Cu and W) to an electrically insulating substrate, which is considerably hard to fabricate electronic devices and then unambiguously measure the intrinsic electronic properties of borophene. Therefore, efficient strategies for preparing larger and high-quality 2D B nanosheets remain to be developed in the future, and then can be easily transferred for practical device applications, especially for anisotropic device applications. Besides, more experiments should be carried out to reveal the undiscovered properties of 2D borophene, and then boost its fast development in the practical applications.

Chemically, borophene possesses a comparatively high stability in the air at RT, although oxidation is suppressed when exposed to pure O_2 under ultrahigh vacuum conditions [87, 174, 182]. However, it is more easily oxidized by oxygen at a high temperature (600–700 °C), especially for 3-dimensional B structures. What's more, when the thickness of B layers decreases to few-layer or even mono-layer height, the oxidation of B only occurs at the edges of the layers, and the terrace of B remains excellent without damage [189]. Unfortunately, the degradation nature of borophene still remains unclear so far, and it's possible that the oxidation process might be speeded up by some other atmospheric species, such as moisture and illumination, which is known for boron thin films [192].

2.2.2 *Anisotropic properties of borophene*

Since the remained challenges face the efficient synthesis, the current research concerning about the anisotropic properties of borophene is still stayed in the stage of theorectical calculation. Previously, Cui et al. [193] predicted a novel 2D all-boron phase (π phase) that can be stably grown on the tungsten surfaces (W (110)), which was studied by phonon and molecular dynamics (MD) simulation. They also revealed that the conductivity along the *x*-direction is about 4 times greater than that along the *y*-direction for the π phase 2D B with highly anisotropic crystal structure at 300 K. The anisotropic conductivity was resulted from different bonding analysis, that is, the *x*-direction contains a continuous arrangement of delocalized π bonds, while along the *y*-direction, the π bonds are separated by 2c-2e σ bonds. Normally continuous delocalized π bonding arrangement results in a prominently larger conductivity in *x*-direction, which makes the π phase 2D B flakes a promising anisotropic electric material, like Fig. 10(c) shows.

The special and unique structure of borophene results in substantial anisotropy of mechanical properties. Different from other 2D materials with covalent bonds, borophene consists of multicenter bonds, which can exhibit unique mechanical response within the elastic limits. The curve of ideal tensile stress and engineering strain for triangular boron flake is shown in Fig. 10(d). When at a relatively small strain, the boron flake exhibits a linear stress-strain relationship, with conspicuous elastic anisotropy. While as the strain increases, the stress-strain relationship becomes nonlinear increasing and shows more obvious anisotropy. And the stress peak reaches up to around 20.9 $N \cdot m^{-1}$ along the ridges at ε_{xx} = 8.7%, while 12.2 $N \cdot m^{-1}$ at ε_{yy} = 14.3% across the ridges [175]. However, for some other kinds of 2D boron sheets which possess intrinsic negative phonon frequencies, such as $\nu_{1/6}$ and $\nu_{1/8}$ sheets, they may show a little anisotropy for obscuring the appearance of negative frequency induced by strain. Owing to the strong and highly coordinated B–B bonds, the Young's modulus in-plane is around 170 GPa·nm along the *x*-direction, while 398 GPa·nm along the *y*-direction in theory (Fig. 10(e)), which can potentially rival the graphene of about 340 GPa·nm [87]. What's more, the out of plane buckling of borophene leads to anisotropic negative Poisson's ratio in plane (Fig. 10(f)), that is, around −0.02 along the *x*-direction and −0.04 along the *y*-direction, which results in unusual mechanical properties, such as in-plane expansion under tensile strain [184]. The highly anisotropic nature of mechanical properties of borophene should be originated from the phenomenon that the B–B bond along the *x*-direction possesses the highest strength than that in other directions.

Apart from the mechanical properties, Zhou et al. [178] studied the thermal conductance properties of monolayer borophene by the methods of first-principles calculations and the non-equilibrium Green's function simulations. They demonstrated that the thermal conductance of borophene, both hexagonal and β_{12} models, are highly anisotropic. At RT, for the hexagonal model, the lattice thermal conductance of boron along the *x*-direction (7.87 $nW \cdot K^{-1} \cdot nm^{-2}$) was around two times higher than that along the *y*-direction (4.89 $nW \cdot K^{-1} \cdot nm^{-2}$), as shown in Fig. 10(g). While for β_{12} model boron, the saturated thermal conductance along the *x*-direction (10.97 $nW \cdot K^{-1} \cdot nm^{-2}$) was about three times higher than that along the *y*-direction (3.30 $nW \cdot K^{-1} \cdot nm^{-2}$), as shown in Fig. 10(h). Remarkably, the highest thermal conductance can reach 7.87 and 10.97 $nW \cdot K^{-1} \cdot nm^{-2}$ for hexagonal and β_{12} models at RT, respectively, which are significantly higher than that of isotropic graphene (5.10 $nW \cdot K^{-1} \cdot nm^{-2}$). Interestingly, it should be pointed out that borophene is the only 2D material with higher thermal conductance than that of graphene, compared with other discovered 2D materials till now.

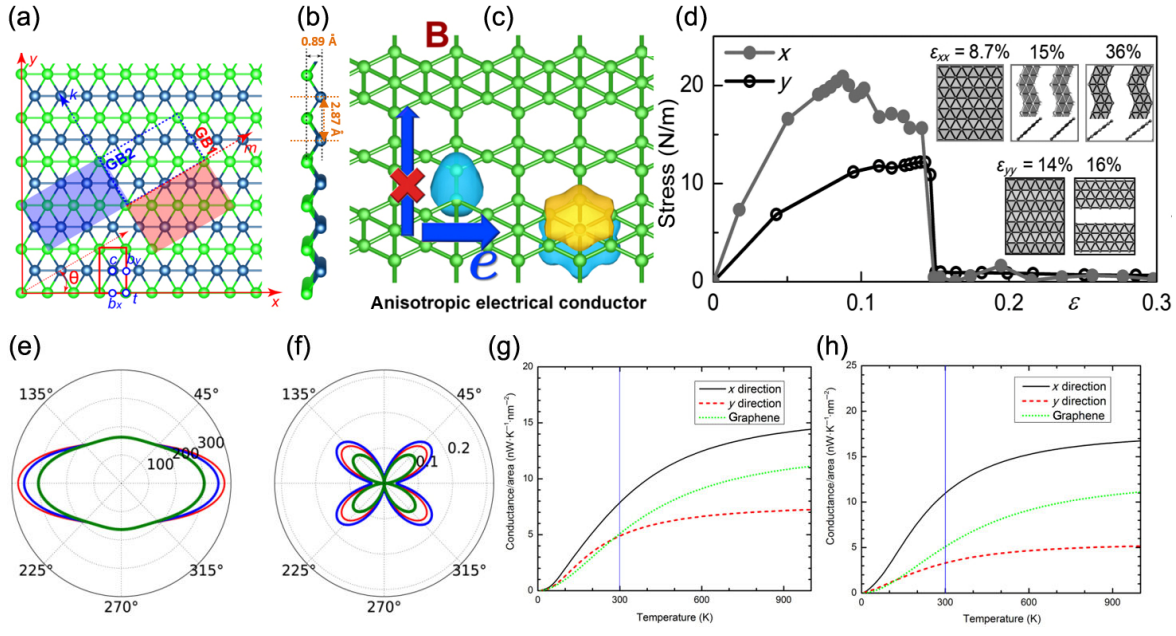

Figure 10 (a) Top and (b) side views of the monolayer Borophene. (c) π phase boron layer grown on a W (110) surface predicted to possess anisotropic electrical property. (Reproduced with permission from Ref. [193], © American Chemical Society 2017). (d) Tensile stress as a function of uniaxial strain in *x* and *y*-directions for the triangular borophene. (Reproduced with permission from Ref. [175], © WILEY-VCH Verlag GmbH & Co. KGaA, Weinheim 2017). (e) Calculated orientation-dependent Youngs's modulus $Y(\theta)$ and (f) Poisson's ratio $\nu(\theta)$. (Reproduced with permission from Ref. [86], © American Chemical Society 2017). (g) and (h) Thermal conductance of hexagonal and β12 Borophene, respectively. (Reproduced with permission from Ref. [178], © Zhou, H. B. et al. 2017).

2.3 Anisotropic 2D-TMDs

Some significant electronic and photoelectronic devices based on the anisotropic 2D TMDs are summarized below.

Rhenium disulfide [73, 74] and rhenium diselenide [75] (ReS_2 and $ReSe_2$) are two kinds of semiconducting TMDs that were recently proved to hold weak coupling between layers and a unique twisted 1T structure. Similar with other TMDs, ReS_2 and $ReSe_2$ show the crystal structure with strong covalent in-plane bonds while weak van der Waals between interlayers. The crystal structure of side view and top view of monolayer ReS_2 are shown in Figs. 11(a) and 11(b), and it contains two hexagonal planes of S (blue) and an intercalated hexagonal plane of Re (green) bound with S forming chains of parallelogram-shaped Re clusters. Therefore, layered ReS_2 is one of the most desirable 2D candidate for studying semiconducting TMDs with low-symmetry. Such asymmetric structure endow ReS_2 many anisotropic properties, such as anisotropic electrical and optical properties. Besides that, the distorted $CdCl_2$ layer structure of ReS_2 causes triclinic symmetry and obvious in-plane anisotropy, which is significantly different from any other TMDs with hexagonal structures like MoS_2. The intrinsic anisotropy of ReS_2 and $ReSe_2$ provides many possibilities to control its anisotropic properties for novel applications.

The $ReSe_2$ crystals were firstly prepared through a wet reaction method from Re_2Se_7 under vacuum at 325 °C [36]. Then the layered bulk $ReSe_2$ crystals was directly synthesized through vapor transport at high temperature with the help of a halide carrier to improve the crystallinity [37]. However, the prepared ReS_2 and $ReSe_2$ flakes were too small in lateral size (micrometers) to be used in the mechanically exfoliated study. Then, the synthesis of larger size layered ReS_2 was realized by spurred CVD method from high purity elemental powders [38]. Keyshar et al. synthesized monolayer ReS_2 through a CVD method from sulfur and ammonium perrhenate at considerably low temperatures (450 °C) [39]. Besides, Fujita et al. [40] synthesized the ReS_2 layers by using liquid exfoliation through lithium borohydride intercalation method.

As we all know that ReS_2 is a stable n-type semiconductor with tunable in-plane anisotropy. In 2015, Lin et al. [74] proved both in experiment and theory calculations that the high performance of single-layer ReS_2 transistor with current on/off ratio as high as 1×10^6 and mobility up to 23.1 $cm^2 \cdot V^{-1} \cdot s^{-1}$ along the higher conduction direction, is an order of magnitude difference along the lower conduction direction. And the linear dichroism in layered ReS_2 induced by its anisotropic structure makes it possible for us to study the polarization sensitive photodetector. The polarization of the incident light is dominated through the combination of a polarizer and a half wave plate. Figure 11(c) clearly reveals the evolution between photocurrent and the polarization angle of the linear polarizer. When setting the incident power to a fixed value, the photocurrent changes dramatically by rotating the polarization of the light. Importantly, the photocurrent along the *b*-axis (defined as 90°) is much larger than that perpendicular to the *b*-axis (defined as 0°) with the incident light polarized changing. This is an obvious evidence that proves the polarization dependent light absorption and photocurrent detection through linear dichroism. The variation of the photocurrent at the drain voltage of 1, 2 and 3 V with the polarization angle of the incident light is shown in Fig. 3(e). The obtained data can be fitted by a sinusoidal equation perfectly. And the dependence of photocurrent and absorption on the polarization of incident light is very similar, as shown in Fig. 11(f) which are put in the same polar graphic. This strongly suggests that the intrinsic polarization-related optical response just originates from ReS_2 itself. All these results mentioned above clearly demonstrate the intrinsically anisotropic nature of the ReS_2 crystal structure, when the incident light in different polarization states passing through the sample.

In 2016, Zhang et al. [195] reported the successful synthesis of $ReSe_2$ nanosheets onto SiO_2 and h-BN substrates by CVD method and fabricated photodetectors to study their polarization sensitive photoresponsivity. Typically, layered $ReSe_2$ possesses a distorted 1T structure and the cluster of Re_4 units forms a

1D chain inside each monolayer as shown in Fig. 12(a). There are two principle crystal axes corresponding to the shortest (*b*-axis) and second-shortest axis (*a*-axis) in the basal plane. Figure 12(b) and its inset are the corresponding high-resolution TEM image and selected area electron diffraction pattern of layered $ReSe_2$ that verify the single-crystalline characteristics. As schematically displayed in Fig. 12(c), the unpolarized photodetection behavior of the device was probed by a focused laser beam of 633 nm with an illumination power ranging from 1 to 20 μW. Figure 12(e) shows the large-area photocurrent images for the whole channel under different polarization directions of the incident laser (Fig. 12(d)). With the continuous rotation of polarized light from 0° to 90°, the photocurrent reaches its maximum value when the incident light is polarized along the *b* crystal axis (0° polarization) and reaches its minimum at the perpendicular setup (90°

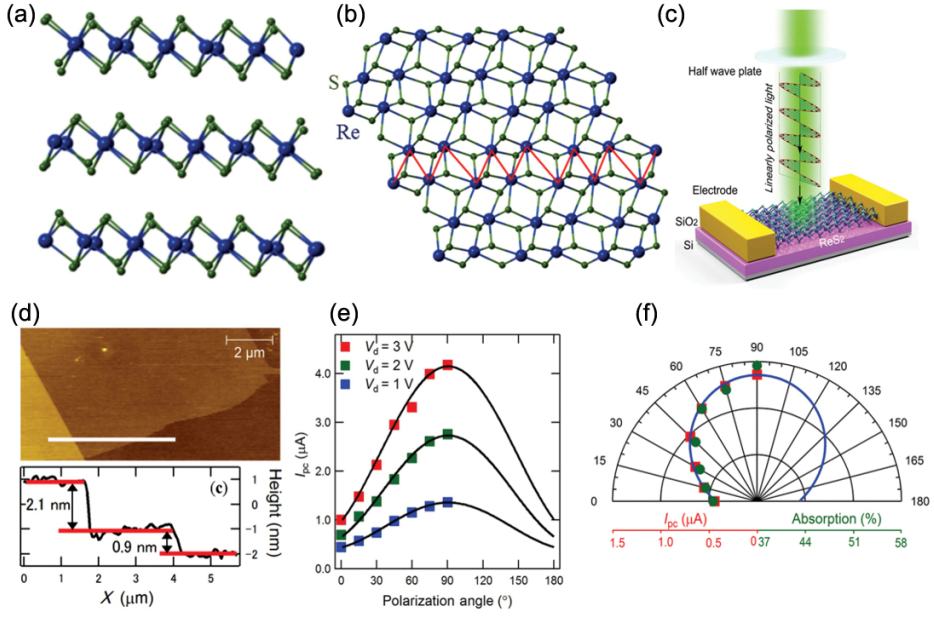

Figure 11 Crystal structure and TEM characteristics of the ReS_2. (a) Side view and (b) top view of the crystal structure. (c) 3D schematic view of the photo-detection device. (d) An AFM image of $ReSe_2$ and the line profile of the ReS_2 flake along the white line. (e) The change of the photocurrent under different drain biases plotted as a function of polarization angle. (f) The photocurrent with drain bias of 1 V (red squire) and absorption (green circle) measured under different polarization angle of green light and plotted in polar coordinates. (Reproduced with permission from Ref. [194], © WILEY-VCH Verlag GmbH & Co. KGaA, Weinheim 2016).

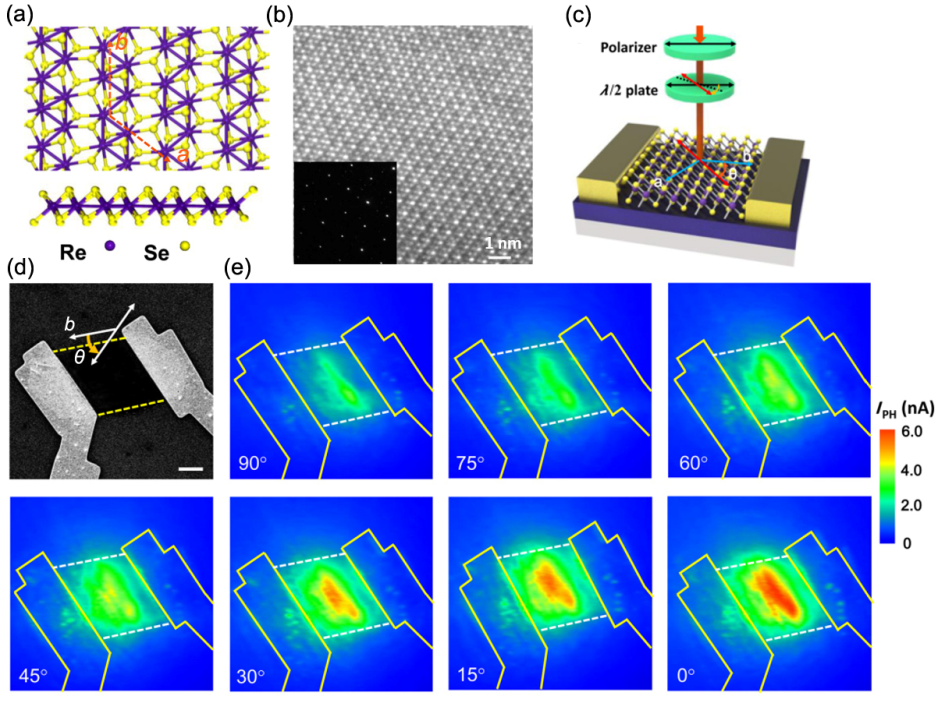

Figure 12 (a) (Top) Top view of the crystal structure of $ReSe_2$. Red dashed line, *a*-axis and *b*-axis of $ReSe_2$ crystal. (Bottom) Side view of monolayer $ReSe_2$. (b) High-resolution TEM image. Inset: corresponding electron diffraction pattern. (c) Schematic structure of $ReSe_2$ photodetectors. The laser was set to pass through a linear polarizer, and then a half-wave plate was used to change the polarization direction, θ here stands for angle between the laser polarization direction and *b*-axis of $ReSe_2$. (d) SEM image of the $ReSe_2$ photodetector; the source-drain electrodes are along *b*-axis of the $ReSe_2$ crystal. θ is the same angle as shown in (c). (e) Polarization-dependent photocurrent mapping of the device, showing prominent linear dichroic photodetection. The thickness of the $ReSe_2$ channel is 12 nm. (Reproduced with permission from Ref. [195], © American Chemical Society 2016).

polarization). Such phenomena unambiguously demonstrated that the incident laser with different polarization directions encountered a varying absorption when it travelled across the $ReSe_2$ channel, which reflects the intrinsically anisotropic nature of the $ReSe_2$ crystals.

2.4 Anisotropic Group IV monochalcogenides

The chemical formula of group IV monochalcogenides compounds can be expressed as MX (M = Ge or Sn and X = S or Se), including the SnSe, SnS, GeSe, and GeS, which show the similar puckered structures like BP (Figs. 13(a) and 13(b)). And all these compounds are isoelectronic and have orthorhombic crystal structure held together by van der Waals interaction with eight atoms in one-unit cell, four of each species. All atoms around are threefold coordinated and tetrahedral coordination caused by the repulsion of the lone pairs [197]. Additionally, 2D group IV monochalcogenides compounds are less toxic, earth-abundant, environmental compatibility and possess suitable and wide bandgaps (1.6–1.7 eV for GeS, 1.1–1.2 eV for GeSe, 1.18–1.66 eV for SnS and 1.0–1.1 eV for SnSe) [198]. And the bandgaps of group IV monochalcogenides are layer dependent and will decrease from 1.44–2.32 eV (monolayer) to 1.00–1.24 eV (bulk) with the increasing thickness. What's more, the compounds may translate to the direct bandgap semiconductors when suffered from a small tensile strain below 3% [199].

Bulk MX have been widely investigated in the field of thermoelectric and photovoltaic applications owing to their unique thermoelectric and optical properties [200]. In 1932, Hofmann et al. [201] synthesized the SnS crystals by a melt growth method. Although many previous reviews have reported on how to synthesize bulk and thin films of SnS crystals in experimental, the method of preparing monolayer SnS had not been mentioned yet. In 1956 and 1958, Okazaki et al. prepared both SnSe [202] and GeSe [203] crystals through heating the corresponding elements above their melting point, and then cooled the melting sample to the RT slowly. Later, large and variable thickness of SnS 2D flakes were prepared on mica surface via physical vapor deposition (PVD) method. SnS bilayer has been proven by liquid exfoliation in NMP solvents by Brent et al. [204]. Ramasamy et al. [205] have proposed several different methods to prepare SnS flakes including CVD method assisted by organometallic aerosol as precursors for the synthesis of vertically aligned SnS flakes. However, monolayer SnS films were not explored so far. Importantly, this CVD method may be a promising route for scalable synthesis of 2D SnS in the future.

Comparing with BP and its group-V phosphorene analogues, group IV monochalcogenides compounds are more stable in chemical properties [198, 206]. Yu Guo et al. [198] proved it via the first-principles calculations that monolayer group-IV monochalcogenides possess excellent oxidation resistance with activation energies within 1.26–1.60 eV for the chemisorption of O_2 on the 2D materials, which is about twice of that for phosphorene and arsenene, indicating a much slower oxidation

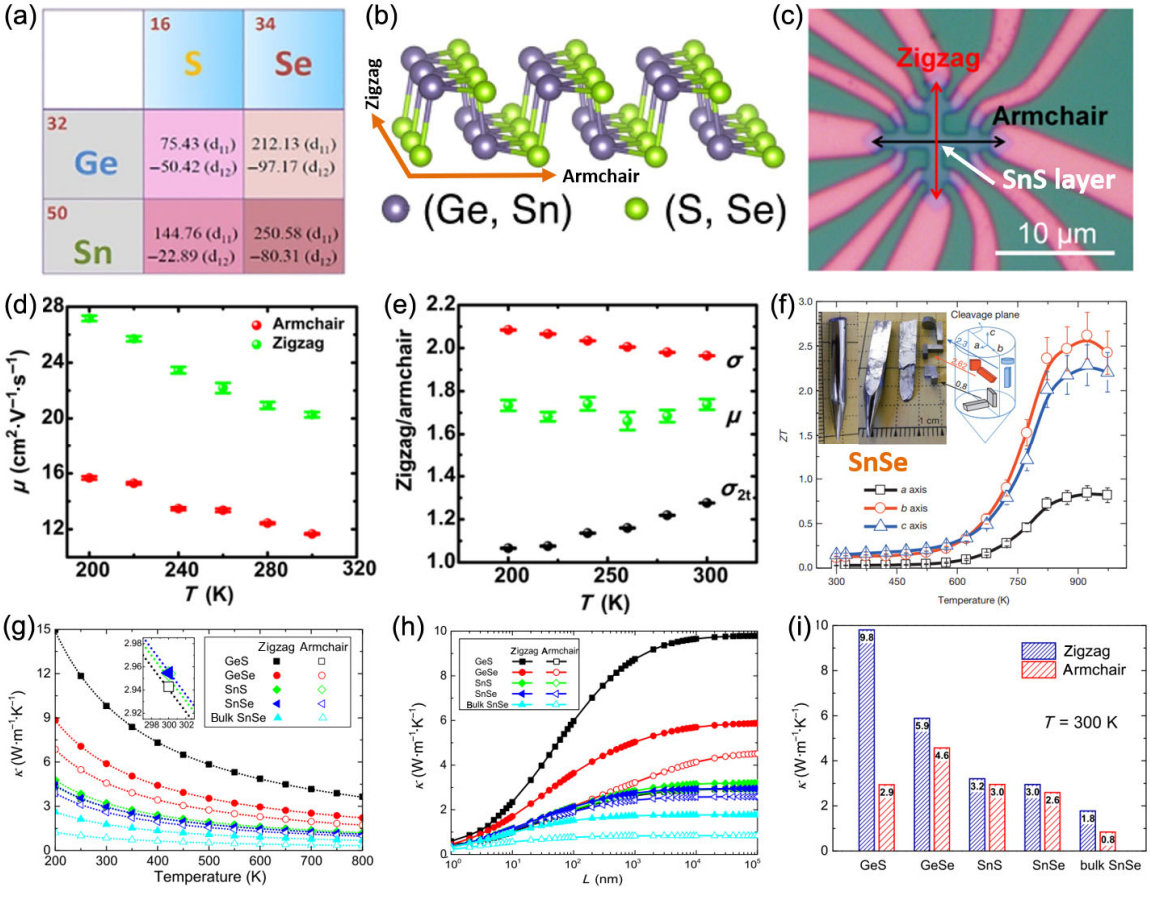

Figure 13 Elemental composition (a) and crystal structure (b) of group IV monochalcogenides. (c) Optical image of a 12.8 nm SnS FET on 300 nm SiO_2/Si. (d) Mobility at zero gate voltage. (e) Temperature dependent ratio of mobility, μ; four-terminal sheet conductivity, σ; and two-terminal conductivity, σ_{2t}, between the ZZ and AC directions. (Reproduced with permission from Ref. [82], © American Chemical Society 2017). (f) Main panel, ZT values along different axial directions of SnSe. (Reproduced with permission from Ref. [28], © Macmillan Publishers Limited 2014). (g) k as a function of temperature ranging from 200 to 800 K. (h) The lattice thermal conductivity for different thickness of group IV monochalcogenides at 300 K. (i) Anisotropic k along ZZ and AC directions at 300 K for the four monolayer compounds and bulk SnSe. (Reproduced with permission from Ref. [196], © The Royal Society of Chemistry 2016).

rate. The activation energy of monolayer group-IV monochalcogenides is comparable to that of monolayer MoS_2 (1.59 eV) with a good oxidation resistance for O_2 chemisorption [207]. Water in the environment is another very important factor to accelerate BP oxidation [117–119, 208]. The activation energy of O_2 chemisorption for phosphorene is 0.58 eV, which is about 0.12 eV lower than that only with O_2, indicating that humid environment will accelerate the oxidation of phosphorene. However, the activation energy (1.32 eV) for oxygen dissociation on monolayer GeS in the presence of O_2 and H_2O is only slightly higher than that without H_2O by 0.06 eV, which indicates H_2O does not influence the oxidization behavior of the monolayer GeS. Higher chemical stability in ambient condition makes group IV monochalcogenides compounds have a bright future to fabricate high-performance photoelectric and thermoelectric devices.

The anisotropy of group IV monochalcogenides in-plane crystal structure is mainly caused by the low lattice symmetry, which is shown in Fig. 13(b), and the different connection ways along the *x*-axis and *y*-axis result in their low in-plane lattice symmetry. In order to measure the anisotropic electrical transport of the as prepared SnS nanoplates, a multi-terminal FET device with a cross Hall-bar structure was fabricated by electron beam lithography (EBL) and H_2 plasma etching method, as shown in Fig. 13(c). The ZZ and AC directions were firstly confirmed by the polarized Raman spectroscopy marked in Fig. 13(c). Tian at el. [82] proved that the carrier mobility along the ZZ direction was up to 20 $cm^2 \cdot V^{-1} \cdot s^{-1}$, which was 1.7 times higher than that along the AC direction at RT. Temperature-dependent carrier mobility along the ZZ and AC directions was calculated to quantitatively observe the anisotropic electrical property, as shown in Fig. 13(d). Note that the ZZ direction always has a higher mobility, and mobilities along the ZZ and AC directions are both increasing with the reduction of temperature, remaining obvious anisotropic electrical property. Temperature dependent ratios of mobility (μ), four-terminal sheet conductivity (σ) and two-terminal conductivity (σ_{2t}) between the ZZ and AC directions are pelted in Fig. 13(e), which all shows conspicuous anisotropy, especially for the mobility as high as 2. Additionally, the mobility ratio between the ZZ and AC direction has a little increment with the temperature decreases, while another two ratios are not. In 2014, Zhao at el. [28] investigated the ultralow thermal conductivity on SnSe crystals and demonstrated that the thermal conductivity of SnSe is intrinsically anisotropic, resulting in the ZT = 2.62 along the *b* axis, ZT = 2.3 along the *c* axis, and ZT = 0.8 along the *a* axis at 923 K in Fig. 13(f). Qin at el. [196] studied the diversely anisotropic properties of 2D group IV monochalcogenides via the first-principles calculations, such as phonon velocity, Young's modulus and thermal conductivity. All the monolayer group IV monochalcogenides (GeS, GeSe, SnS and SnSe) exhibit obvious anisotropic thermal conductivity property, as shown in the Fig. 13(i). In particular, the thermal conductivity (k) along the ZZ and AC directions of monolayer GeS shows the strongest anisotropy and the anisotropic thermal ratio is as high as 3.38. Both the thermal conductivity and anisotropic thermal ratios are temperature (Fig. 13(g)) and thickness (Fig. 13(h)) dependent. In addition, the calculated k at different temperatures from 200 to 800 K decreases as the temperature increases, while the calculated k decreases with the increase of thickness of group IV monochalcogenides shown in Fig. 13(h). Moreover, it is also demonstrated that the anisotropic thermal conductivity would be influenced by the limited size. With finite size, the k value and the anisotropy could be effectively lowered and adjusted by nanofabrication, which may help to extend the applications in nanoscale thermoelectric and thermal management.

3 Overview of anisotropic properties for some representative anisotropic 2D materials

Table 1 is the anisotropic electricity and photoelectric properties of some representative anisotropic 2D materials. It can be seen from the Table 1 that all the listed 2D materials possess a higher carrier mobility along the ZZ direction than AC direction. Black-As has the highest carrier mobility ratio as high as 28.10, then is the black-AsP up to 11.75. While for few-layers BP, the carrier mobility ratio is as low as 1.50. The carrier mobility ratio is between 1.50 and 4.00 for most of material except black As and black-AsP. Although the carrier mobility ratio is not so high, few-layers BP possess the highest absolute carrier mobility up to 1,000 $cm^2 \cdot V^{-1} \cdot s^{-1}$ along the ZZ direction and 600 $cm^2 \cdot V^{-1} \cdot s^{-1}$ along the AC direction, which is very important for the electrical and optoelectronic devices application. Therefore, for the practical device applications in the future, it is necessary to take a full consideration to coordinate absolute carrier mobility and carrier mobility ratio to meet a better electrical and optoelectronic properties.

Table 1 Anisotropic electricity and photoelectric properties of some representative anisotropic 2D materials

Materials	Test condition	Carrier mobility ($cm^2 \cdot V^{-1} \cdot s^{-1}$)		Carrier mobility ratio (ZZ/AC)	Ref.
		ZZ direction	AC direction		
BP (~ 30 nm)	RT photo-detector, FET	μ_x = 1.5 μ_y	μ_y	1.50	[18]
Monolayer BP	RT, photoluminescence (PL)	Big	Small	—	[71]
BP (~ 10 nm)	RT, FET	1,000	600	1.67	[88, 209]
Few-layers GeP	RT, FET	Extracted anisotropic factor σ_x, $R\lambda x$ =*I*phx.	Σ_y =1.52σ_x, $R\lambda y$ =*I*phy = 1.83	1.52	[168]
Monolayer black-AsP	RT, first-principles calculations, FET	μ_x = 11.75μ_y	μ_y	11.75	[210]
Black-As	RT, FET	376.7	13.4	28.10	[100, 211]
2D Boron (π phase)	RT, phonon and molecular dynamics simulation	μ_x = 4μ_y	μ_y	4.00	[193]
Single-layer ReS_2	RT photo-detector, FET	Along the DS-chains = 23.1	Crossing the DS-chains = 14.8	1.56	[74]
Few-layers ReS_2	RT photo-detector, FET	μ_x = 3.1μ_y	μ_y	3.10	[73]
GeS (170 nm)	RT, Photoluminescence (PL)	Big	Small	—	[80]
2D SnS nanoplates	RT, FET	20	11.76	1.70	[82]

Table 2 is a summary of anisotropic thermoelectric properties of some representative anisotropic 2D materials. Layered ReS_2 has the highest thermal conductance up to 18.58 $nW{\cdot}k^{-1}{\cdot}nm^{-2}$ along the ZZ direction and simultaneously highest thermal conductance ratio as high as 26.9 among all the 2D anisotropic materials. For layered BP, the ZZ direction have a higher thermal conductance than AC direction, and the thermal conductance ratio along ZZ and AC is around 2.00. Interestingly, the absolute thermal conductance is layer dependent, but the thermal conductance ratio is not. Comparing with BP layers, both hexagonal model and β12 model boron, have a higher thermal conductance along the AC direction than along the ZZ direction, which is different from that of anisotropic electricity and photoelectric properties. For boron, β12 model boron possesses a smaller thermal conductance ratio than hexagonal model Boron, but shows more obvious anisotropy in thermal conductance. For monolayer group IV monochalcogenides, GeS possesses the highest thermal conductance and thermal conductance ratio in theory.

When it comes to anisotropic mechanical properties in Table 3, all 2D materials have a higher young's modulus along the ZZ direction than along the AC direction. Borophene shows the highest absolute young's modulus both along ZZ direction (398 GPa) and AC direction (170 GPa). Although the monolayer GeS has the lowest absolute young's modulus along two directions, the highest young's modulus ratio between ZZ and AC direction can be up to 3.81, The Young's modulus ratios for different forms of BP are ranging from 2.15 (few-layer BP) to 2.57 (single-layer BP), which is a little bit higher than that of Borophene. At the same time, it can be noted that the group IV monochalcogenides exhibit weaker absolute Young's modulus than BP and borophene, especially for monolayer GeS.

Besides anisotropic 2D materials, many other low-symmetry materials also possess excellent anisotropic optical, electrical and photoelectric properties, enabling their applications in anisotropic devices. Among them, 1D and quasi-1D materials, like nanorods, nanowires, nanofibers and nanoribbons, are the mostly studied. In 2016, Wu et al. [213] has reported a 1D MoS_2 nanoribbons (width between 5 nm to 15 nm) with high anisotropic optical properties caused by the 1D quantum confinement effect. Polarized Raman behavior observed on the 1D MoS_2 nanoribbons is attributed to the anisotropic light absorption. In 2018, Liu et al. [214] demonstrated a quasi-1D titanium trisulfide (TiS_3) based photodetectors. The photo-responsivity ratio on the polarization direction of the device can highly reach 4:1, which is coming from the reduced in-plane structural symmetry of the TiS_3. In 2018, Niu et al. [215] reported a quasi-1D single-crystal barium titanium sulfide ($BaTiS_3$), whose atoms are arranged in parallel chain-like structures. Polarized infrared absorption spectroscopy show that the absorption edge of $BaTiS_3$ would blue shift to 1.6 μm (0.76 eV) when the polarization was perpendicular to the *c* axis. Although 1D and quasi-1D materials possess good anisotropic optoelectronic properties, for device fabrication,

Table 2 Anisotropic thermoelectric properties of some representative anisotropic 2D materials

Materials	Test condition	Thermal conductance ($nW{\cdot}K^{-1}{\cdot}nm^{-2}$)		Thermal conductance ratio (ZZ/AC)	Ref.
		ZZ direction	AC direction		
Monolayer BP	From 200 to 400 K First-principles calculations	Big	Small	—	[27]
BP nanoribbons	Above 100 K In experiment	$k_x = k_y + 7$	k_y	—	[103]
BP layers (Above 15 nm)	In experiment by micro-Raman spectroscopy	40	20	2.00	[93]
BP layers (9.5 nm)	In experiment by micro-Raman spectroscopy	20	10	2.00	[93]
hexagonal model Boron	RT, first-principles calculations	4.89	7.87	0.62	[178]
β12 model boron	RT, first-principles calculations	3.30	10.97	0.30	[178]
$ReSe_2$	RT, first-principles calculations	18.58	0.69	26.9	[212]
Monolayer GeS	RT, first-principles calculations	9.81	2.94	3.38	[196]
Monolayer GeSe	RT, first-principles calculations	5.89	4.57	1.28	[196]
Monolayer SnS	RT, first-principles calculations	3.21	2.95	1.07	[196]
Monolayer SnSe	RT, first-principles calculations	2.95	2.59	1.15	[196]

Table 3 Anisotropic machinal properties of some representative anisotropic 2D materials

Materials	Test condition	Young's modulus		Young's modulus ratio (ZZ/AC)	Ref.
		ZZ direction	AC direction		
Single-layer BP	First-principles calculations	56.3 $N{\cdot}m^{-1}$	21.9 $N{\cdot}m^{-1}$	2.57	[155]
Few-layer BP	AFM nanoindentation	58.6 GPa	27.2 GPa	2.15	[102]
Suspended BP nanoribbons	AFM nanoindentation	65 GPa	27 GPa	2.41	[94]
BP nano resonators	Finite element modeling	116.1 GPa	46.5 GPa	2.50	[151]
Boron ($\nu_{1/6}$ and $\nu_{1/8}$)	First-principles calculations	398 GPa	170 GPa	2.34	[87]
Boron (triangular nanosheet)	First-principles calculations	20.9 $N{\cdot}m^{-1}$	12.2 $N{\cdot}m^{-1}$	1.71	[175]
Monolayer GeS	First-principles calculations	29.74 GPa	7.8 GPa	3.81	[196]
Monolayer GeSe	First-principles calculations	54.63 GPa	22.10 GPa	2.47	[196]
Monolayer SnS	First-principles calculations	44.11 GPa	25.30 GPa	1.74	[196]
Monolayer SnSe	First-principles calculations	45.14 GPa	23.72 GPa	1.90	[196]

it is hard to fabricate multi-group symmetrical electrodes on the small diameter surface of 1D and quasi-1D materials. In this case, 2D materials might be a better solution for high performances anisotropic devices fabrication, especially for their mass production in the future.

4 Conclusions and perspectives

Over the past few years, around the anisotropic 2D materials, the achievements in device designs, integration, mechanical analysis, and micro-/nano-fabrication techniques have boosted the development of soft electronics, printable electronics and optoelectronics applications, especially for the flexible and stretchable systems, including FETs [124, 169, 216], sensors [140, 158, 217], actuators, light emitting diode [13, 218], polarization-sensitive photodetector [152, 219, 220], photovoltaics and bare die integrated circuits. Such in-plane or out-plane anisotropic characteristics not only endow the 2D layered materials richer physical properties, but also provide the researchers another perspective for tuning the electrical, optical, mechanical and thermal properties. Meanwhile, anisotropic 2D materials can also widen the scope of opportunities for designing novel 2D semiconductor devices and exploring distinctive applications, although there mightily exist some potential challenges aiming to achieve desirable performance. Basically, the discovery of emerging anisotropic 2D materials, as well as the study of their physical properties concerning about in-plane anisotropy is not only of scientific importance but also technological requirement. However, the practical applications for anisotropic 2D materials in the future still face great challenges and have a long way to go.

Firstly, it is well known that the micromechanical cleavage is still the most commonly applied method to fabricate the highest quality 2D crystals layers for 2D materials research and device applications. However, such strategy suffers an ultralow yield, which makes the scalability of applications up to industrial level to be difficult. While for vapor-based deposition, those techniques usually need a high productive cost, as well as the complicated process parameters, and the required high growth temperature (> 400 °C) which is incompatible with some device fabrication processes. Besides, the additional transfer step of 2D materials to other substrates is necessary for device applications. On the other hand, although the LPE approaches have the merits of extremely low cost and strong controllability, the obtained 2D materials with poor crystal quality and small area seems not to be suitable for the device applications. Therefore, the method to fabricate large-area, cost-effective, highly controllable, high-quality, single-crystal anisotropic 2D material with desired structures is still not mature enough, which greatly limit the scalable and reproducible device fabrication in practical applications, especially for designing and controlling the anisotropic properties. However, if the high-quality growth of anisotropic 2D materials on silicon wafers by vapor deposition under low temperature conditions with a relatively simple process parameters could be achieved, vapor deposition technology would have great application potential for large-scale production in devices.

Secondly, the construction of vertical and lateral hetero-junctions based on anisotropic 2D layered materials have opened a new research field and unfolded avenues for novel material manufacturing in nanomaterial science and nano device applications. The weak vdW force during interlayers allows us to isolate anisotropic 2D monolayer and restack them into arbitrary stacking heterojunctions without the consideration of atomic comparability when in their bulk counterparts. What's more, anisotropic heterojunctions could be formed by stacking two or three different anisotropic 2D layered materials through mechanical stacking method and CVD method, where structure of the electronic band near the interface will be changed according to static electricity. For anisotropic 2D materials, there are more combination possible when two or three kinds of different 2D materials are stoichiometrically stacked together to form heterojunctions. Then, the better performance (electronic, optoelectronic, thermoelectric and nanomechanical) of the heterojunction can be realized by adjusting the combining direction of 2D materials. Therefore, the study of anisotropic 2D materials-based heterojunctions is not only important and meaningful for the theoretical research, but also has special significance for practical device applications in the future.

Thirdly, advanced theoretical researches on anisotropic 2D materials are urgently needed, as well as computing tools and software, which are very important for guiding the experiment researches and practical applications. Accurate and reliable theoretical predictions can not only speed up experiments in the near future, but also make experiments simpler and instructive. Additionally, more methods and standards related to test and characterize anisotropic properties including electricity, photoelectric, thermoelectric and machinal, should be proposed and developed to ensure that the method of achieving anisotropy is simpler, quicker, more accurate and reliable. If so, it will save a lot of time and encourage more researchers to study the field of anisotropic 2D materials.

Finally, other materials systems, such as 1D, 2D and 3D materials, can be rationally introduced to integrate with anisotropic 2D materials for achieving the practical device applications, which can improve their anisotropic performance to some extent. However, there is still a huge challenge to integrate the 2D materials with other materials without damaging their lattice structure or altering the intrinsic electronic, optoelectronic, thermoelectric and nanomechanical properties. Therefore, new method should be put forward to void the lattice mismatch during the integration, aiming to maximumly realize the synergistic performance on the basis of retaining their own original properties.

In summary, anisotropic 2D materials have many excellent physical and chemical properties and different kinds of anisotropic 2D materials can be restacked to compose diverse heterostructures, which can bring up unlimited possibilities for the development of various anisotropic devices in the future. However, the controllable preparation of high quality anisotropic 2D materials, the mechanism of the physical properties of the anisotropic heterostructures and the uncertain changes in physicochemical properties of anisotropic 2D materials, are still needed to be solved before a series of practical device applications on anisotropic 2D materials have been realized.

5 Acknowledgements

This work is supported by the State Key Research Development Program of China (No. 2019YFB2203503), the National Natural Science Foundation of China (Nos. 61875138, 61961136001, 61435010, and U1801254), the Guangdong Science Foundation for Distinguished Young Scholars (No. 2018B030306038), the Science and Technology Innovation Commission of Shenzhen (Nos. JCYJ20180507182047316, KQJSCX20180328095501798, KQTD2015032416270385, and GJHZ20180928160209731), the Natural Science Foundation of SZU (No. 860-000002110429), the Educational Commission of Guangdong Province (Nos. 2016KCXTD006 and 2018KCXTD026), and the Science and

Technology Development Fund (Nos. 007/2017/A1 and 132/2017/A3), Macao SAR, China.

References

[1] Novoselov, K. S.; Geim, A. K.; Morozov, S. V.; Jiang, D.; Zhang, Y.; Dubonos, S. V.; Grigorieva, I. V.; Firsov, A. A. Electric field effect in atomically thin carbon films. *Science* **2004**, *306*, 666–669.

[2] Jiang, X. T.; Liu, S. X.; Liang, W. Y.; Luo, S. J.; He, Z. L.; Ge, Y. Q.; Wang, H. D.; Cao, R.; Zhang, F.; Wen, Q. et al. Broadband nonlinear photonics in few-layer MXene $Ti_3C_2T_x$ (T = F, O, or OH). *Laser Photonics Rev*. **2018**, *12*, 1700229.

[3] Ge, Y. Q.; Zhu, Z. F.; Xu, Y. H.; Chen, Y. X.; Chen, S.; Liang, Z. M.; Song, Y. F.; Zou, Y. S.; Zeng, H. B.; Xu, S. X. et al. Broadband nonlinear photoresponse of 2D TiS_2 for ultrashort pulse generation and all-optical thresholding devices. *Adv. Opt. Mater*. **2018**, *6*, 1701166.

[4] Song, Y. F.; Liang, Z. M.; Jiang, X. T.; Chen, Y. X.; Li, Z. J.; Lu, L.; Ge, Y. Q.; Wang, K.; Zheng, J. L; Lu, S. B. et al. Few-layer antimonene decorated microfiber: Ultra-short pulse generation and all-optical thresholding with enhanced long term stability. *2D Mater*. **2017**, *4*, 045010.

[5] Du, J.; Zhang, M.; Guo, Z.; Chen, J.; Zhu, X.; Hu, G.; Peng, P.; Zheng, Z.; Zhang, H. Phosphorene quantum dot saturable absorbers for ultrafast fiber lasers. *Sci. Rep*. **2017**, *7*, 42357.

[6] Guo, B.; Wang, S. H.; Wu, Z. X.; Wang, Z. X.; Wang, D. H.; Huang, H.; Zhang, F.; Ge, Y. Q.; Zhang, H. Sub-200 fs soliton mode-locked fiber laser based on bismuthene saturable absorber. *Opt. Express* **2018**, *26*, 22750–22760.

[7] Li, P. F.; Chen, Y.; Yang, T. S.; Wang, Z. Y.; Lin, H.; Xu, Y. H.; Li, L.; Mu, H. R.; Shivananju, B. N.; Zhang, Y. P. et al. Two-dimensional $CH_3NH_3PbI_3$ perovskite nanosheets for ultrafast pulsed fiber lasers. *ACS Appl. Mater. Interfaces* **2017**, *9*, 12759–12765.

[8] Zheng, J. L.; Yang, Z. H.; Chen, S.; Liang, Z. M.; Chen, X.; Cao, R.; Guo, Z. N.; Wang, K.; Zhang, Y.; Ji, J. H. et al. Black phosphorus based all-optical-signal-processing: Toward high performances and enhanced stability. *ACS Photonics* **2017**, *4*, 1466–1476.

[9] Wang, Y. Z.; Huang, W. C.; Wang, C.; Guo, J.; Zhang, F.; Song, Y. F.; Ge, Y. Q.; Wu, L. M.; Liu, J.; Li, J. Q. et al. An all-optical, actively Q-switched fiber laser by an antimonene-based optical modulator. *Laser Photonics Rev*. **2019**, *13*, 1800313.

[10] Wang, C.; Wang, Y. Z.; Jiang, X. T.; Xu, J. W.; Huang, W. C.; Zhang, F.; Liu, J. F.; Yang, F. M.; Song, Y. F.; Ge, Y. Q. et al. MXene $Ti_3C_2T_x$: A promising photothermal conversion material and application in all-optical modulation and all-optical information loading. *Adv. Opt. Mater*. **2019**, *7*, 1900060.

[11] Wang, Y. Z.; Zhang, F.; Tang, X.; Chen, X.; Chen, Y. X.; Huang, W. C.; Liang, Z. M.; Wu, L. M.; Ge, Y. Q.; Song, Y. F. et al. All-optical phosphorene phase modulator with enhanced stability under ambient conditions. *Laser Photonics Rev*. **2018**, *12*, 1800016.

[12] Zheng, J. L.; Tang, X.; Yang, Z. H.; Liang, Z. M.; Chen, Y. X.; Wang, K.; Song, Y. F.; Zhang, Y.; Ji, J. H.; Liu, Y. et al. Few-layer phosphorene-decorated microfiber for all-optical thresholding and optical modulation. *Adv. Opt. Mater*. **2017**, *5*, 1700026.

[13] Wu, L. M.; Huang, W. C.; Wang, Y. Z.; Zhao, J. L.; Ma, D. T.; Xiang, Y. J.; Li, J. Q.; Ponraj, J. S.; Dhanabalan, S. C.; Zhang, H. 2D tellurium based high-performance all-optical nonlinear photonic devices. *Adv. Funct. Mater*. **2019**, *29*, 1806346.

[14] Wang, X. M.; Xia, F. N. Black phosphorus optoelectronics. In *Proceedings of 2016 Conference on Lasers and Electro-Optics*, San Jose, USA, 2016, pp. 1–2.

[15] Dhanabalan, S. C.; Ponraj, J. S.; Guo, Z. N.; Li, S. J.; Bao, Q. L.; Zhang, H. Emerging trends in phosphorene fabrication towards next generation devices. *Adv. Sci*. **2017**, *4*, 1600305.

[16] Singh, E.; Singh, P.; Kim, K. S.; Yeom, G. Y.; Nalwa, H. S. Flexible molybdenum disulfide (MoS_2) atomic layers for wearable electronics and optoelectronics. *ACS Appl. Mater. Interfaces* **2019**, *11*, 11061–11105.

[17] Bablich, A.; Kataria, S.; Lemme, M. C. Graphene and two-dimensional materials for optoelectronic applications. *Electronics* **2016**, *5*, 13.

[18] Xia, F. N.; Wang, H.; Jia, Y. C. Rediscovering black phosphorus as an anisotropic layered material for optoelectronics and electronics. *Nat. Commun*. **2014**, *5*, 1158.

[19] Yang, P. F.; Zhang, Z. P.; Sun, M. X.; Lin, F.; Cheng, T.; Shi, J. P.; Xie, C. Y.; Shi, Y. P.; Jiang, S. L.; Huan, Y. H. et al. Thickness tunable wedding-cake-like MoS_2 flakes for high-performance optoelectronics. *ACS Nano* **2019**, *13*, 3649–3658.

[20] Lee, H. S.; Min, S. W.; Chang, Y. G.; Park, M. K.; Nam, T.; Kim, H.; Kim, J. H.; Ryu, S.; Im, S. MoS_2 nanosheet phototransistors with thickness-modulated optical energy gap. *Nano Lett*. **2012**, *12*, 3695–3700.

[21] Haratipour, N.; Namgung, S.; Oh, S. H.; Koester, S. J. Fundamental limits on the subthreshold slope in schottky source/drain black phosphorus field-effect transistors. *ACS Nano* **2016**, *10*, 3791–3800.

[22] Wang, Y. M.; Ding, K.; Sun, B. Q.; Lee, S. T.; Jie, J. S. Two-dimensional layered material/silicon heterojunctions for energy and optoelectronic applications. *Nano Res*. **2016**, *9*, 72–93.

[23] Huo, N. J.; Konstantatos, G. Ultrasensitive all-2D MoS_2 phototransistors enabled by an out-of-plane MoS_2 PN homojunction. *Nat. Commun*. **2017**, *8*, 572.

[24] Xu, Y. J.; Yuan, J.; Zhang, K.; Hou, Y.; Sun, Q.; Yao, Y. M.; Li, S. J.; Bao, Q. L.; Zhang, H.; Zhang, Y. G. Field-induced n-doping of black phosphorus for CMOS compatible 2D logic electronics with high electron mobility. *Adv. Funct. Mater*. **2017**, *27*, 1702211.

[25] Dhanabalan, S. C.; Ponraj, J. S.; Guo, Z. N.; Li, S. J.; Bao, Q. L.; Zhang, H. Emerging trends in phosphorene fabrication towards next generation devices. *Adv. Sci*. **2017**, *4*, 1600305.

[26] Zhang, Y. P.; Lim, C. K.; Dai, Z. G.; Yu, G. N.; Haus, J. W.; Zhang, H.; Prasad, P. N. Photonics and optoelectronics using nano-structured hybrid perovskite media and their optical cavities. *Phys. Rep*. **2019**, *795*, 1–51.

[27] Fei, R. X.; Faghaninia, A.; Soklaski, R.; Yan, J. A.; Lo, C.; Yang, L. Enhanced thermoelectric efficiency via orthogonal electrical and thermal conductances in phosphorene. *Nano Lett*. **2014**, *14*, 6393–6399.

[28] Zhao, L. D.; Lo, S. H.; Zhang, Y. S.; Sun, H.; Tan, G. J.; Uher, C.; Wolverton, C.; Dravid, V. P.; Kanatzidis, M. G. Ultralow thermal conductivity and high thermoelectric figure of merit in SnSe crystals. *Nature* **2014**, *508*, 373–377.

[29] Lee, M. J.; Ahn, J. H.; Sung, J. H.; Heo, H.; Jeon, S. G.; Lee, W.; Song, J. Y.; Hong, K. H.; Choi, B.; Lee, S. H. et al. Thermoelectric materials by using two-dimensional materials with negative correlation between electrical and thermal conductivity. *Nat. Commun*. **2016**, *7*, 12011.

[30] Anasori, B.; Lukatskaya, M. R.; Gogotsi, Y. 2D metal carbides and nitrides (MXenes) for energy storage. *Nat. Rev. Mater*. **2017**, *2*, 16098.

[31] Luo, B.; Wang, B.; Li, X. L.; Jia, Y. Y.; Liang, M. H.; Zhi, L. J. Graphene-confined Sn nanosheets with enhanced lithium storage capability. *Adv. Mater*. **2012**, *24*, 3538–3543.

[32] Zhou, L.; Zhuang, Z. C.; Zhao, H. H.; Lin, M. T.; Zhao, D. Y.; Mai, L. Q. Intricate hollow structures: Controlled synthesis and applications in energy storage and conversion. *Adv. Mater*. **2017**, *29*, 1602914.

[33] Xue, Y. H.; Zhang, Q.; Wang, W. J.; Cao, H.; Yang, Q. H.; Fu, L. Opening two-dimensional materials for energy conversion and storage: A concept. *Adv. Energy Mater*. **2017**, *7*, 1602684.

[34] Qiu, M.; Sun, Z. T.; Sang, D. K.; Han, X. G.; Zhang, H.; Niu, C. M. Current progress in black phosphorus materials and their applications in electrochemical energy storage. *Nanoscale* **2017**, *9*, 13384–13403.

[35] Xie, Z. J.; Xing, C. Y.; Huang, W. C.; Fan, T. J.; Li, Z. J.; Zhao, J. L.; Xiang, Y. J.; Guo, Z. N.; Li, J. Q.; Yang, Z. G. et al. Ultrathin 2D nonlayered tellurium nanosheets: Facile liquid-phase exfoliation, characterization, and photoresponse with high performance and enhanced stability. *Adv. Funct. Mater*. **2018**, *28*, 1705833.

[36] Li, Y.; Wang, R. H.; Guo, Z. N.; Xiao, Z.; Wang, H. D.; Luo, X. L.; Zhang, H. Emerging two-dimensional noncarbon nanomaterials for flexible lithium-ion batteries: Opportunities and challenges. *J. Mater. Chem. A* **2019**, *7*, 25227–25246.

[37] Wang, R. H.; Li, X. H.; Wang, Z. X.; Zhang, H. Electrochemical analysis graphite/electrolyte interface in lithium-ion batteries: P-Toluenesulfonyl isocyanate as electrolyte additive. *Nano Energy* **2017**, *34*, 131–140.

[38] Ren, X. H.; Zhou, J.; Qi, X.; Liu, Y. D.; Huang, Z. Y.; Li, Z. J.; Ge, Y. Q.; Dhanabalan, S. C.; Ponraj, J. S.; Wang, S. Y. et al. Few-layer

black phosphorus nanosheets as electrocatalysts for highly efficient oxygen evolution reaction. *Adv. Energy Mater.* **2017**, *7*, 1700396.
[39] Duan, J. J.; Chen, S.; Jaroniec, M.; Qiao, S. Z. Heteroatom-doped graphene-based materials for energy-relevant electrocatalytic processes. *ACS Catal.* **2017**, *5*, 5207–5234.
[40] Wang, H.; Jiang, S. L.; Shao, W.; Zhang, X. D.; Chen, S. H.; Sun, X, S.; Zhang, Q.; Luo, Y.; Xie, Y. Optically switchable photocatalysis in ultrathin black phosphorus nanosheets. *J. Am. Chem. Soc.* **2018**, *140*, 3474–3480.
[41] Tan, X.; Tahini, H. A.; Smith, S. C. p-doped graphene/graphitic carbon nitride hybrid electrocatalysts: Unraveling charge transfer mechanisms for enhanced hydrogen evolution reaction performance. *ACS Catal.* **2016**, *6*, 7071–7077.
[42] Sotelo-Vazquez, C.; Quesada-Cabrera, R.; Ling, M.; Scanlon, D. O.; Kafizas, A.; Thakur, P. K.; Lee, T. L.; Taylor, A.; Watson, G. W.; Palgrave, R. G. et al. Photocatalysis: Evidence and effect of photogenerated charge transfer for enhanced photocatalysis in WO_3/TiO_2 heterojunction films: A computational and experimental study. *Adv. Funct. Mater.* **2017**, *27*, 1605413.
[43] Wang, H. B.; Maiyalagan, T.; Wang, X. Review on recent progress in nitrogen-doped graphene: Synthesis, characterization, and its potential applications. *ACS Catal.* **2012**, *2*, 781−794.
[44] Fu, Q.; Bao X. H. Surface chemistry and catalysis confined under two-dimensional materials. *Chem. Soc. Rev.* **2017**, *46*, 1842–1874.
[45] Deng, D. H.; Novoselov, K. S.; Fu, Q.; Zheng, N.; Tian, Z. Q.; Bao, X. H. Catalysis with two-dimensional materials and their heterostructures. *Nat. Nanotechnol.* **2016**, *11*, 218–230.
[46] Sun, Z. B.; Xie, H. H.; Tang, S. Y.; Yu, X. F.; Guo, Z. N.; Shao, J. D.; Zhang, H.; Huang, H.; Wang, H. Y.; Chu, P. K. Ultrasmall black phosphorus quantum dots: Synthesis and use as photothermal agents. *Angew. Chem., Int. Ed.* **2015**, *54*, 11526–11530.
[47] Shao, J. D.; Xie, H. H.; Huang, H.; Li, Z. B.; Sun, Z. B.; Xu, Y. H.; Xiao, Q. L.; Yu, X. F.; Zhao, Y. T.; Zhang, H. et al. Biodegradable black phosphorus-based nanospheres for *in vivo* photothermal cancer therapy. *Nat. Commun.* **2016**, *7*, 12967.
[48] Chen, W. S.; Ouyang, J.; Liu, H.; Chen, M.; Zeng, K.; Sheng, J. P.; Liu, Z. J.; Han, Y. J.; Wang, L. Q.; Li, J. et al. Black phosphorus nanosheet-based drug delivery system for synergistic photodynamic/photothermal/chemotherapy of cancer. *Adv. Mater.* **2017**, *29*, 1603864.
[49] Tao, W.; Zhu, X. B.; Yu, X. H.; Zeng, X. W.; Xiao, Q. L.; Zhang, X. D.; Ji, X. Y.; Wang, X. S.; Shi, J. J; Zhang, H. et al. Black phosphorus nanosheets as a robust delivery platform for cancer theranostics. *Adv. Mater.* **2017**, *29*, 1603276.
[50] Qiu, M.; Wang, D.; Liang, W. Y.; Liu, L. P.; Zhang, Y.; Chen, X.; Sang, D. K.; Xing, C. Y.; Li, Z. J.; Dong, B. Q. et al. Novel concept of the smart NIR-light-controlled drug release of black phosphorus nanostructure for cancer therapy. *Proc. Natl. Acad. Sci. USA* **2018**, *115*, 501–506.
[51] Xie, H. H.; Li, Z. B.; Sun, Z. B.; Shao, J. D.; Yu, X. F.; Guo, Z. N.; Wang, J. H.; Xiao, Q. L.; Wang, H. Y.; Wang, Q. Q. et al. Metabolizable ultrathin Bi_2Se_3 nanosheets in imaging-guided photothermal therapy. *Small* **2016**, *12*, 4136–4145.
[52] Ji, X. Y.; Kong, N.; Wang, J. Q.; Li, W. L.; Xiao, Y. L.; Gan, S. T.; Zhang, Y.; Li, Y. J.; Song, X. R.; Xiong, Q. Q. et al. A novel top-down synthesis of ultrathin 2D boron nanosheets for multimodal imaging-guided cancer therapy. *Adv. Mater.* **2018**, *30*, 1803031.
[53] Luo, M. M.; Fan, T. J.; Zhou, Y.; Zhang, H.; Mei, L. 2D black phosphorus–based biomedical applications. *Adv. Funct. Mater.* 2019, *29*, 1808306.
[54] Zhang, M.; Wu, Q.; Zhang, F.; Chen, L. L.; Jin, X. X.; Hu, Y. W.; Zheng, Z.; Zhang, H. 2D Black phosphorus saturable absorbers for ultrafast photonics. *Adv. Opt. Mater.* **2019**, *7*, 1800224.
[55] Liang, X.; Ye, X. Y.; Wang, C.; Xing, C. Y.; Miao, Q. W.; Xie, Z. J.; Chen, X. L.; Zhang, X. D.; Zhang, H.; Mei, L. Photothermal cancer immunotherapy by erythrocyte membrane-coated black phosphorus formulation. *J. Control. Release* **2019**, *296*, 150–161.
[56] Xue, T. Y.; Liang, W. Y.; Li, Y. W.; Sun, Y. H.; Xiang, Y. J.; Zhang, Y. P.; Dai, Z. G.; Duo, Y. H.; Wu, L. M.; Qi, K. et al. Ultrasensitive detection of miRNA with an antimonene-based surface plasmon resonance sensor. *Nat. Commun.* **2019**, *10*, 28.
[57] Tao, W.; Kong, N.; Ji, X. Y.; Zhang, Y. P.; Sharma, A.; Ouyang, J.; Qi, B. W.; Wang, J. Q.; Xie, N.; Kang, C. et al. Emerging two-dimensional monoelemental materials (Xenes) for biomedical applications. *Chem. Soc. Rev.* **2019**, *48*, 2891–2912.
[58] Zhou, Y.; Zhang, M. X.; Guo, Z. N.; Miao, L. L.; Han, S. T.; Wang, Z. Y.; Zhang, X. W.; Zhang, H.; Peng, Z. C. Recent advances in black phosphorus-based photonics, electronics, sensors and energy devices. *Mater. Horiz.* **2017**, *4*, 997–1019.
[59] Mak, K. F.; Lee, C.; Hone, J.; Shan, J.; Heinz, T. F. Atomically thin MoS_2: A new direct-gap semiconductor. *Phys. Rev. Lett.* **2010**, *105*, 136805.
[60] Nair, R. R.; Blake, P.; Grigorenko, A. N.; Novoselov, K. S.; Booth, T. J.; Stauber, T.; Peres, N. M. R.; Geim, A. K. Fine structure constant defines visual transparency of graphene. *Science* **2008**, *320*, 1308.
[61] Tsai, D. S.; Liu, K. K.; Lien, D. H.; Tsai, M. L.; Kang, C. F.; Lin, C. A.; Li, L. J.; He, J. H. Few-layer MoS_2 with high broadband photogain and fast optical switching for use in harsh environments. *ACS Nano* **2013**, *7*, 3905–3911.
[62] Eda, G.; Maier, S. A. Two-dimensional crystals: Managing light for optoelectronics. *ACS Nano* **2013**, *7*, 5660–5665.
[63] Lan, S. F.; Rodrigues, S.; Kang, L.; Cai, W. S. Visualizing optical phase anisotropy in black phosphorus. *ACS Photonics* **2016**, *3*, 1176–1181.
[64] Yun, W. S.; Han, S. W.; Hong, S. C.; Kim, I. G.; Lee, J. D. Thickness and strain effects on electronic structures of transition metal dichalcogenides: 2H-MX_2 semiconductors (M = Mo, W; X = S, Se, Te). *Phys. Rev. B* **2012**, *85*, 033305.
[65] Long, M. S.; Wang, P.; Fang, H. H.; Hu, W. D. Progress, challenges, and opportunities for 2D material based photodetectors. *Adv. Funct. Mater.* **2019**, *29*, 1803807.
[66] Lin, J. J.; Liang, L. B.; Ling, X.; Zhang, S. Q.; Mao, N. N.; Zhang, N.; Sumpter, B. G.; Meunier, V.; Tong, L. M.; Zhang, J. Enhanced Raman scattering on in-plane anisotropic layered materials. *J. Am. Chem. Soc.* **2015**, *137*, 15511–15517.
[67] Wang, Y. L.; Cong, C. X.; Fei, R. X.; Yang, W. H.; Chen, Y.; Cao, B. C.; Yang, L.; Yu, T. Remarkable anisotropic phonon response in uniaxially strained few-layer black phosphorus. *Nano Res.* **2015**, *8*, 3944–3953.
[68] Ling, X.; Huang, S. X.; Hasdeo, E. H.; Liang, L. B.; Parkin, W. M.; Tatsumi, Y.; Nugraha, A. R. T.; Puretzky, A. A.; Das, P. M.; Sumpter, B. G. et al. Anisotropic electron-photon and electron-phonon interactions in black phosphorus. *Nano Lett.* **2016**, *16*, 2260−2267.
[69] Hong, T.; Chamlagain, B.; Lin, W. Z.; Chuang, H. J.; Pan, M. H.; Zhou, Z. X.; Xu, Y. Q. Polarized photocurrent response in black phosphorus field-effect transistors. *Nanoscale* **2014**, *6*, 8978–8983.
[70] Fei, R. X.; Yang, L. Strain-engineering the anisotropic electrical conductance of few-layer black phosphorus. *Nano Lett.* **2014**, *14*, 2884–2889.
[71] Wang, X. M.; Jones, A. M.; Seyler, K. L.; Tran, V.; Jia, Y. C.; Zhao, H.; Wang, H.; Yang, L.; Xu, X. D.; Xia, F. N. Highly anisotropic and robust excitons in monolayer black phosphorus. *Nat. Nanotechnol.* **2015**, *10*, 517–521.
[72] Guo, Z. N.; Zhang, H.; Lu, S. B.; Wang, Z. T.; Tang, S. Y.; Shao, J. D.; Sun, Z. B.; Xie, H. H.; Wang, H. Y.; Yu, X. F. et al. From black phosphorus to phosphorene: Basic solvent exfoliation, evolution of Raman scattering, and applications to ultrafast photonics. *Adv. Funct. Mater.* **2015**, *25*, 6996–7002.
[73] Liu, E. F.; Fu, Y. J.; Wang, Y. J.; Feng, Y. Q.; Liu, H. M.; Wan, X. G.; Zhou, W.; Wang, B. G.; Shao, L. B.; Ho, C. H. et al. Integrated digital inverters based on two-dimensional anisotropic ReS_2 field-effect transistors. *Nat. Commun.* **2015**, *6*, 6991.
[74] Lin, Y. C.; Komsa, H. P.; Yeh, C. H.; Björkman, T.; Liang, Z. Y.; Ho, C. H.; Huang, Y. S.; Chiu, P. W.; Krasheninnikov, A. V.; Suenaga, K. Single-layer ReS_2: Two-dimensional semiconductor with tunable in-plane anisotropy. *ACS Nano* **2015**, *9*, 11249–11257.
[75] Jariwala, B.; Voiry, D.; Jindal, A.; Chalke, B. A.; Bapat, R.; Thamizhavel, A.; Chhowalla, M.; Deshmukh, M.; Bhattacharya, A. Synthesis and characterization of ReS_2 and $ReSe_2$ layered chalcogenide single crystals. *Chem. Mater.* **2016**, *28*, 3352–3359.
[76] Ma, D. T.; Zhao, J. L.; Wang, R.; Xing, C. Y.; Li, Z. J.; Huang, W. C.; Jiang, X. T.; Guo, Z. N.; Luo, Z. Q.; Li, Y. et al. Ultrathin GeSe nanosheets: From systematic synthesis, to studies of carrier dynamics and applications for high-performance UV-Vis photo-detector. *ACS*

Appl. Mater. Interfaces **2019**, *11*, 4278–4287.
[77] Xue, D. J.; Tan, J. H.; Hu, J. S.; Hu, W. P.; Guo, Y. G.; Wan, L. J. Anisotropic photoresponse properties of single micrometer-sized GeSe nanosheet. *Adv. Mater.* **2012**, *24*, 4528–4533.
[78] Gomes, L. C.; Carvalho, A. Phosphorene analogues: Isoelectronic two-dimensional group-IV monochalcogenides with orthorhombic structure. *Phys. Rev. B* **2015**, *92*, 085406.
[79] Hu, T.; Dong, J. M. Two new phases of monolayer group-IV monochalcogenides and their piezoelectric properties. *Phys. Chem. Chem. Phys.* **2016**, *18*, 32514–32520.
[80] Tan, D. Z.; Lim, H. E.; Wang, F. J.; Mohamed, N. B.; Mouri, S.; Zhang, W. J.; Miyauchi, Y.; Ohfuchi, M.; Matsuda, K. Anisotropic optical and electronic properties of two-dimensional layered germanium sulfide. *Nano Res.* **2017**, *10*, 546–555.
[81] Li, X. Z.; Xia, J.; Wang, L.; Gu, Y. Y.; Cheng, H. Q.; Meng, X. M. Layered SnSe nano-plates with excellent in-plane anisotropic properties of Raman spectrum and photo-response. *Nanoscale* **2017**, *9*, 14558–14564.
[82] Tian, Z.; Guo, C. L.; Zhao, M. X.; Li, R. R.; Xue, J. M. Two-dimensional SnS: A phosphorene analogue with strong in-plane electronic anisotropy. *ACS Nano* **2017**, *11*, 2219–2226.
[83] Wang, X. T.; Li, Y. T.; Huang, L.; Jiang, X. W.; Jiang, L.; Dong, H. L.; Wei, Z. M.; Li, J. B.; Hu, W. P. Short-wave near-infrared linear dichroism of two-dimensional germanium selenide. *J. Am. Chem. Soc.* **2017**, *139*, 14976–14982.
[84] Liu, J.; Pantelides, S. T. Anisotropic thermal expansion of group-IV monochalcogenide monolayers. *Appl. Phys. Express* **2018**, *11*, 101301.
[85] Mannix, A. J.; Zhang, Z. H.; Guisinger, N. P.; Yakobson, B. I.; Hersam, M. C. Borophene as a prototype for synthetic 2D materials development. *Nat. Nanotechnol.* **2018**, *13*, 444–450.
[86] Wang, V.; Geng, W. T. Lattice defects and the mechanical anisotropy of borophene. *J. Phys. Chem. C* **2017**, *121*, 10224–10232.
[87] Piazza, Z. A.; Hu, H. S.; Li, W. L.; Zhao, Y. F.; Li, J.; Wang, L. S. Planar hexagonal B(36) as a potential basis for extended single-atom layer boron sheets. *Nat. Commun.* **2014**, *5*, 1–6.
[88] Li, L. K.; Yu, Y. J.; Ye, G. L.; Ge, Q. Q.; Ou, X. D.; Wu, H.; Feng, D. L.; Chen, X. H.; Zhang, Y. B. Black phosphorus field-effect transistors. *Nat. Nanotechnol.* **2014**, *9*, 372–377.
[89] Du, Y. C.; Liu, H.; Deng, Y. X.; Ye, P. D. Device perspective for black phosphorus field-effect transistors: Contact resistance, ambipolar behavior, and scaling. *ACS Nano* **2014**, *8*, 10035–10042.
[90] Liu, H.; Neal, A. T.; Zhu, Z.; Luo, Z.; Xu, X. F.; Tománek, D.; Ye, P. D. Phosphorene: An unexplored 2D semiconductor with a high hole mobility. *ACS Nano* **2014**, *8*, 4033–4041.
[91] Qiao, J. S.; Kong, X. H.; Hu, Z. X.; Yang, F.; Ji, W. High-mobility transport anisotropy and linear dichroism in few-layer black phosphorus. *Nat. Commun.* **2014**, *5*, 4475.
[92] Kim, J.; Baik, S. S.; Ryu, S. H.; Sohn, Y.; Park, S.; Park, B. G.; Denlinger, J.; Yi, Y.; Choi, H. J.; Kim, K. S. Observation of tunable band gap and anisotropic dirac semimetal state in black phosphorus. *Science* **2015**, *349*, 723–726.
[93] Luo, Z.; Maassen, J.; Deng, Y. X.; Du, Y. C.; Garrelts, R. P.; Lundstrom, M. S.; Ye, P. D.; Xu, X. F. Anisotropic in-plane thermal conductivity observed in few-layer black phosphorus. *Nat. Commun.* **2015**, *6*, 8572.
[94] Chen, H.; Huang, P.; Guo, D.; Xie, G. X. Anisotropic mechanical properties of black phosphorus nanoribbons. *J. Phys. Chem. C* **2016**, *120*, 29491–29497.
[95] Wang, Y.; Xu, G. Z.; Hou, Z. P.; Yang, B. C.; Zhang, X. M.; Liu, E. K.; Xi, X. K.; Liu, Z. Y.; Zeng, Z. M.; Wang, W. H. et al. Large anisotropic thermal transport properties observed in bulk single crystal black phosphorus. *Appl. Phys. Lett.* **2016**, *108*, 092102.
[96] Liu, X. L.; Ryder, C. R.; Wells, S. A.; Hersam, M. C. Resolving the in-plane anisotropic properties of black phosphorus. *Small Methods* **2017**, *1*, 1700143.
[97] Chen, S.; Cheng, Y.; Zhang, G.; Pei, Q. X.; Zhang, Y. W. Anisotropic wetting characteristics of water droplets on phosphorene: Roles of layer and defect engineering. *J. Phys. Chem. C* **2018**, *122*, 4622–4627.
[98] Jiang, H.; Shi, H. Y.; Sun, X. D.; Gao, B. Optical anisotropy of few-layer black phosphorus visualized by scanning polarization modulation microscopy. *ACS Photonics* **2018**, *5*, 2509–2515.
[99] Yang, H.; Jussila, H.; Autere, A.; Komsa, H. P.; Ye, G. J.; Chen, X. H.; Hasan, T.; Sun, Z. P. Optical waveplates based on birefringence of anisotropic two-dimensional layered materials. *ACS Photonics* **2017**, *4*, 3023–3030.
[100] Chen, Y. B.; Chen, C. Y.; Kealhofer, R.; Liu, H. L.; Yuan, Z. Q.; Jiang, L. L.; Suh, J.; Park, J.; Ko, C.; Choe, H. S. et al. Black arsenic: A layered semiconductor with extreme in-plane anisotropy. *Adv. Mater.* **2018**, *30*, 1800754.
[101] Wu, J. X.; Mao, N. N.; Xie, L. M.; Xu, H.; Zhang, J. Identifying the crystalline orientation of black phosphorus using angle-resolved polarized Raman spectroscopy. *Angew. Chem.* **2015**, *127*, 2396–2399.
[102] Tao, J.; Sheng, W. F.; Wu, S.; Liu, L.; Feng, Z. H.; Wang, C.; Hu, C. G.; Yao, P.; Zhang, H.; Pang, W. et al. Mechanical and electrical anisotropy of few-layer black phosphorus. *ACS Nano* **2015**, *9*, 11362–11370.
[103] Lee, S.; Yang, F.; Suh, J.; Yang, S. J.; Lee, Y.; Li, G.; Choe, H. S.; Suslu, A.; Chen, Y. B.; Ko, C. et al. Anisotropic in-plane thermal conductivity of black phosphorus nanoribbons at temperatures higher than 100 K. *Nat. Commun.* **2015**, *6*, 8573.
[104] Zhao, J. L.; Zhu, J. J.; Cao, R.; Wang, H. D.; Guo, Z. N.; Sang, D. K.; Tang, J. N.; Fan, D. Y.; Li, J. Q.; Zhang, H. Liquefaction of water on the surface of anisotropic two-dimensional atomic layered black phosphorus. *Nat. Commun.* **2019**, *10*, 4062.
[105] Bridgman, P. W. Two new modifications of phosphorus. *J. Am. Chem. Soc.* **1914**, *36*, 1344–1363.
[106] Hultgren, R.; Gingrich, N. S.; Warren, B. E. The atomic distribution in red and black phosphorus and the crystal structure of black phosphorus. *J. Chem. Phys.* **1935**, *3*, 351–355.
[107] Maruyama, Y.; Suzuki, S.; Kobayashi, K.; Tanuma, S. Synthesis and some properties of black phosphorus single crystals. *Physica B+C* **1981**, *105*, 99–102.
[108] Endo, S.; Akahama, Y.; Terada, S. I.; Narita, S. I. Growth of large single crystals of black phosphorus under high pressure. *Jpn. J. Appl. Phys.* **1982**, *21*, L482–L484.
[109] Shirotani, I. Growth of large single crystals of black phosphorus at high pressures and temperatures, and its electrical properties. *Mol. Cryst. Liq. Cryst.* **1982**, *86*, 203–211.
[110] Krebs, V. H.; Schultze-Gebhardt, F. Über die struktur und eigenschaften der halbmetalle. VII. neubestimmung der struktur des glasigen selens nach verbesserten röntgenographischen methoden. *Acta Crystallogr.* **1955**, *8*, 412–419.
[111] Liu, H.; Du, Y. C.; Deng, Y. X.; Ye, P. D. Semiconducting black phosphorus: Synthesis, transport properties and electronic applications. *Chem. Soc. Rev.* **2015**, *44*, 2732–2743.
[112] Nilges, T.; Kersting, M.; Pfeifer, T. A fast low-pressure transport route to large black phosphorus single crystals. *J. Solid State Chem.* **2008**, *181*, 1707–1711.
[113] Köpf, M.; Eckstein, N.; Pfister, D.; Grotz, C.; Krüger, I.; Greiwe, M.; Hansen, T.; Kohlmann, H.; Nilges, T. Access and *in situ* growth of phosphorene-precursor black phosphorus. *J. Cryst. Growth* **2014**, *405*, 6–10.
[114] Li, X. S.; Deng, B. C.; Wang, X. M.; Chen, S. Z.; Vaisman, M.; Karato, S. I.; Pan, G.; Lee, M. L.; Cha, J.; Wang, H. et al. Synthesis of thin-film black phosphorus on a flexible substrate. *2D Mater.* **2015**, *2*, 031002.
[115] Sang, D. K.; Wang, H. D.; Guo, Z. N.; Xie, N.; Zhang, H. Recent developments in stability and passivation techniques of phosphorene toward next-generation device applications. *Adv. Funct. Mater.* **2019**, *29*, 1903419.
[116] Pei, J. J.; Gai, X.; Yang, J.; Wang, X. B.; Yu, Z. F.; Choi, D. Y.; Luther-Davies, B.; Lu, Y. R. Producing air-stable monolayers of phosphorene and their defect engineering. *Nat. Commun.* **2016**, *7*, 10450.
[117] Zhao, Y. T.; Wang, H. Y.; Huang, H.; Xiao, Q. L.; Xu, Y. H.; Guo, Z. N.; Xie, H. H.; Shao, J. D.; Sun, Z. B.; Han, W. J. et al. Surface coordination of black phosphorus for robust air and water stability. *Angew. Chem., Int. Ed.* **2016**, *55*, 5003–5007.
[118] Zhou, Q. H.; Chen, Q.; Tong, Y. L.; Wang, J. L. Light-induced ambient degradation of few-layer black phosphorus: Mechanism and protection. *Angew. Chem., Int. Ed.* **2016**, *55*, 11437–11441.
[119] Abellán, G.; Wild, S.; Lloret, V.; Scheuschner, N.; Gillen, R.; Mundloch, U.; Maultzsch, J.; Varela, M.; Hauke, F.; Hirsch, A.

Fundamental insights into the degradation and stabilization of thin layer black phosphorus. *J. Am. Chem. Soc.* **2017**, *139*, 10432–10440.
[120] Avsar, A.; Tan, J. Y.; Luo, X.; Khoo, K. H.; Yeo, Y.; Watanabe, K.; Taniguchi, T.; Quek, S. Y.; Ozyilmaz, B. Van der waals bonded Co/h-BN contacts to ultrathin black phosphorus devices. *Nano Lett.* **2017**, *17*, 5361–5367.
[121] Zhu, H.; McDonnell, S.; Qin, X. Y.; Azcatl, A.; Cheng, L. X.; Addou, R.; Kim, J.; Ye, P. D.; Wallace, R. M. Al_2O_3 on black phosphorus by atomic layer deposition: An *in situ* interface study. *ACS Appl. Mater. Interfaces* **2015**, *7*, 13038–13043.
[122] Luo, X.; Rahbarihagh, Y.; Hwang, J. C. M.; Liu, H.; Du, Y. C.; Ye, P. D. Temporal and thermal stability of Al_2O_3-passivated phosphorene MOSFETs. *IEEE Electron Device Lett.* **2014**, *35*, 1314–1316.
[123] Kim, J. S.; Liu, Y. N.; Zhu, W. N.; Kim, S.; Wu, D.; Tao, L.; Dodabalapur, A.; Lai, K. J.; Akinwande, D. Toward air-stable multilayer phosphorene thin-films and transistors. *Sci. Rep.* **2015**, *5*, 8989.
[124] Guo, Z. N.; Chen, S.; Wang, Z. Z.; Yang, Z. Y.; Liu, F.; Xu, Y. H.; Wang, J. H.; Yi, Y.; Zhang, H.; Liao, L. et al. Metal-ion-modified black phosphorus with enhanced stability and transistor performance. *Adv. Mater.* **2017**, *29*, 1703811.
[125] Wang, H. D.; Sang, D. K.; Guo, Z. N.; Cao, R.; Zhao, J. L.; Shah, M. N. U.; Fan, T. J.; Fan, D. Y.; Zhang, H. Black phosphorus-based field effect transistor devices for Ag ions detection. *Chin. Phys. B* **2018**, *27*, 087308.
[126] Tang, X.; Liang, W. Y.; Zhao, J. L.; Li, Z. J.; Qiu, M.; Fan, T. J.; Luo, C. S.; Zhou, Y.; Li, Y.; Guo, Z. N. et al. Fluorinated phosphorene: Electrochemical synthesis, atomistic fluorination, and enhanced stability. *Small* **2017**, *13*, 1702739.
[127] Xu, Y. H.; Wang, Z. T.; Guo, Z. N.; Huang, H.; Xiao, Q. L; Zhang, H.; Yu, X. F. Solvothermal synthesis and ultrafast photonics of black phosphorus quantum dots. *Adv. Opt. Mater.* **2016**, *4*, 1223–1229.
[128] Jiang, X. F.; Zeng, Z. K.; Li, S.; Guo, Z. N.; Zhang, H.; Huang, F.; Xu, Q. H. Tunable broadband nonlinear optical properties of black phosphorus quantum dots for femtosecond laser pulses. *Materials* **2017**, *10*, 210.
[129] Lin, C.; Grassi, R.; Low, T.; Helmy, A. S. Multilayer black phosphorus as a versatile mid-infrared electro-optic material. *Nano Lett.* **2016**, *16*, 1683–1689.
[130] Xu, Y. H.; Jiang, X. F.; Ge, Y. Q.; Guo, Z. N.; Zeng, Z. K.; Xu, Q. H.; Zhang, H.; Yu, X. F.; Fan, D. Y. Size-dependent nonlinear optical properties of black phosphorus nanosheets and their applications in ultrafast photonics. *J. Mater. Chem. C* **2017**, 3007–3013.
[131] Liu, J. J.; Liu, J.; Guo, Z. N.; Zhang, H.; Ma, W. W.; Wang, J. Y.; Su, L. B. Dual-wavelength Q-switched Er: SrF_2 laser with a black phosphorus absorber in the mid-infrared region. *Opt. Express* **2016**, *24*, 30289–30295.
[132] Li, C.; Liu, J.; Guo, Z. N.; Zhang, H.; Ma, W. W.; Wang, J. Y.; Xue, X. D.; Su, L B. Black phosphorus saturable absorber for a diode-pumped passively Q-switched Er: CaF_2 mid-infrared laser. *Opt. Commun.* **2018**, *406*, 158–162.
[133] Cao, R.; Wang, H. D.; Guo, Z. N.; Sang, D. K.; Zhang, L. Y.; Xiao, Q. L.; Zhang, Y. P.; Fan, D. Y.; Li, J. Q.; Zhang, H. Black phosphorous/indium selenide photoconductive detector for visible and near-infrared light with high sensitivity. *Adv. Opt. Mater.* **2019**, *7*, 1900020.
[134] Hu, Z. H.; Li, Q.; Lei, B.; Wu, J.; Zhou, Q. H.; Gu, C. D.; Wen, X. L.; Wang, J. Y.; Liu, Y. P.; Li, S. S. et al. Abnormal near-infrared absorption in 2D black phosphorus induced by Ag nanoclusters surface functionalization. *Adv. Mater.* **2018**, *30*, 1801931.
[135] Na, J. H.; Park, K.; Kim, J. T.; Choi, W. K.; Song, Y. W. Air-stable few-layer black phosphorus phototransistor for near-infrared detection. *Nanotechnology* **2017**, *28*, 085201.
[136] Yang, Y. S.; Liu, S. C.; Yang, W.; Li, Z. B.; Wang, Y.; Wang, X.; Zhang, S. S.; Zhang, Y.; Long, M. S.; Zhang, G. M. et al. Air-stable in-plane anisotropic $GeSe_2$ for highly polarization-sensitive photodetection in short wave region. *J. Am. Chem. Soc.* **2018**, *140*, 4150–4156.
[137] Tian, H.; Guo, Q. S.; Xie, Y. J.; Zhao, H.; Li, C.; Cha, J. J.; Xia, F. N.; Wang, H. Anisotropic black phosphorus synaptic device for neuromorphic applications. *Adv. Mater.* **2016**, *28*, 4991–4997.
[138] Yang, G. H.; Wan, X. J.; Gu, Z. P.; Zeng, X. R.; Tang, J. N. Near infrared photothermal-responsive poly(vinyl alcohol)/black phosphorus composite hydrogels with excellent on-demand drug release capacity. *J. Mater. Chem. B* **2018**, *6*, 1622–1632.
[139] Pumera, M. Phosphorene and black phosphorus for sensing and biosensing. *TrAC Trends Anal. Chem.* **2017**, *93*, 1–6.
[140] Lee, G.; Kim, S.; Jung, S.; Jang, S.; Kim, J. Suspended black phosphorus nanosheet gas sensors. *Sensors Actuators B Chem.* **2017**, *250*, 569–573.
[141] Guo, Q. S.; Pospischil, A.; Bhuiyan, M.; Jiang, H.; Tian, H.; Farmer, D.; Deng, B. C.; Li, C.; Han, S. J.; Wang, H. et al. Black phosphorus mid-infrared photodetectors with high gain. *Nano Lett.* **2016**, *16*, 4648–4655.
[142] Zhang, Y. Q.; Dong, N. N.; Tao, H. C.; Yan, C.; Huang, J. W.; Liu, T. F.; Robertson, A. W.; Texter, J.; Wang, J.; Sun, Z. Y. Exfoliation of stable 2D black phosphorus for device fabrication. *Chem. Mater.* **2017**, *29*, 6445–6456.
[143] Youngblood, N.; Li, M. Ultrafast photocurrent measurements of a black phosphorus photodetector. *Appl. Phys. Lett.* **2017**, *110*, 051102.
[144] Flores, E.; Ares, J. R.; Castellanos-Gomez, A.; Barawi, M.; Ferrer, I. J.; Sánchez, C. Thermoelectric power of bulk black-phosphorus. *Appl. Phys. Lett.* **2015**, *106*, 022102.
[145] Chen, X. L.; Lu, X. B.; Deng, B. C.; Sinai, O.; Shao, Y. C.; Li, C.; Yuan, S. F.; Tran, V.; Watanabe, K.; Taniguchi, T. et al. Widely tunable black phosphorus mid-infrared photodetector. *Nat. Commun.* **2017**, *8*, 1672.
[146] Yuan, H. T.; Liu, X. G.; Afshinmanesh, F.; Li, W.; Xu, G.; Sun, J.; Lian, B.; Curto, A. G.; Ye, G. J.; Hikita, Y. et al. Polarization-sensitive broadband photodetector using a black phosphorus vertical p-n junction. *Nat. Nanotechnol.* **2015**, *10*, 707–713.
[147] Jain, A.; McGaughey, A. J. H. Strongly anisotropic in-plane thermal transport in single-layer black phosphorene. *Sci. Rep.* 2015, *5*, 8501.
[148] Qin, G. Z.; Yan, Q. B.; Qin, Z. Z.; Yue, S. Y.; Hu, M.; Su, G. Anisotropic intrinsic lattice thermal conductivity of phosphorene from first principles. *Phys. Chem. Chem. Phys.* **2015**, *17*, 4854–4858.
[149] Cai, Y. Q.; Ke, Q. Q.; Zhang, G.; Feng, Y. P.; Shenoy, V. B.; Zhang, Y. W. Giant phononic anisotropy and unusual anharmonicity of phosphorene: Interlayer coupling and strain engineering. *Adv. Funct. Mater.* **2015**, *25*, 2230–2236.
[150] Smith, B.; Vermeersch, B.; Carrete, J.; Ou, E.; Kim, J.; Mingo, N.; Akinwande, D.; Shi, L. Temperature and thickness dependences of the anisotropic in-plane thermal conductivity of black phosphorus. *Adv. Mater.* **2017**, *29*, 1603756.
[151] Wang, Z. H.; Jia, H.; Zheng, X. Q.; Yang, R.; Ye, G. J.; Chen, X. H.; Feng, P. X. L. Resolving and tuning mechanical anisotropy in black phosphorus via nanomechanical multimode resonance spectromicroscopy. *Nano Lett.* **2016**, *16*, 5394–5400.
[152] Zhu, W. N.; Yogeesh, M. N.; Yang, S. X.; Aldave, S. H.; Kim, J. S.; Sonde, S.; Tao, L.; Lu, N. S.; Akinwande, D. Flexible black phosphorus ambipolar transistors, circuits and AM demodulator. *Nano Lett.* **2015**, *15*, 1883–1890.
[153] Kim, S. K.; Bhatia, R.; Kim, T. H.; Seol, D.; Kim, J. H.; Kim, H.; Seung, W.; Kim, Y.; Lee, Y. H.; Kim, S. W. Directional dependent piezoelectric effect in CVD grown monolayer MoS_2 for flexible piezoelectric nanogenerators. *Nano Energy* **2016**, *22*, 483–489.
[154] Wang, Z. H.; Jia, H.; Zheng, X. Q.; Yang, R.; Wang, Z. F.; Ye, G. J.; Chen, X. H.; Shan, J.; Feng, P. X. L. Black phosphorus nano-electromechanical resonators vibrating at very high frequencies. *Nanoscale* **2015**, *7*, 877–884.
[155] Jiang, J. W.; Park, H. S. Mechanical properties of single-layer black phosphorus. *J. Phys. D Appl. Phys.* **2014**, *47*, 385304.
[156] Wu, W. Z.; Wang, L.; Li, Y. L.; Zhang, F.; Lin, L.; Niu, S. M.; Chenet, D.; Zhang, X.; Hao, Y. F.; Heinz, T. F. et al. Piezoelectricity of single-atomic-layer MoS_2 for energy conversion and piezotronics. *Nature* **2014**, *514*, 470–474.
[157] Wang, Y.; Yang, R.; Shi, Z. W.; Zhang, L. C.; Shi, D. X.; Wang, E. G.; Zhang, G. Y. Super-elastic graphene ripples for flexible strain sensors. *ACS Nano* **2011**, *5*, 3645–3650.
[158] Park, Y. J.; Sharma, B. K.; Shinde, S. M.; Kim, M. S.; Jang, B.; Kim, J. H.; Ahn, J. H. All MoS_2-based large area, skin-attachable active-matrix tactile sensor. *ACS Nano* **2019**, *13*, 3023–3030.

[159] Abbas, A. N.; Liu, B. L.; Chen, L.; Ma, Y. Q.; Cong, S.; Aroonyadet, N.; Köpf, M.; Nilges, T.; Zhou, C. W. Black phosphorus gas sensors. *ACS Nano* **2015**, *9*, 5618–5624.
[160] Liu, B. L.; Köpf, M.; Abbas, A. N.; Wang, X. M.; Guo, Q. S.; Jia, Y. C.; Xia, F. N.; Weihrich, R.; Bachhuber, F.; Pielnhofer, F. et al. Black arsenic-phosphorus: Layered anisotropic infrared semiconductors with highly tunable compositions and properties. *Adv. Mater*. **2015**, *27*, 4423–4429.
[161] Liu, Z.; Ma, L. L.; Shi, G.; Zhou, W.; Gong, Y. J.; Lei, S. D.; Yang, X. B.; Zhang, J. N.; Yu, J. J.; Hackenberg, K. P. et al. In-plane heterostructures of graphene and hexagonal boron nitride with controlled domain sizes. *Nat. Nanotechnol*. **2013**, *8*, 119–124.
[162] Feng, Q. L.; Zhu, Y. M.; Hong, J. H.; Zhang, M.; Duan, W. J.; Mao, N. N.; Wu, J. X.; Xu, H.; Dong, F. L.; Lin, F. et al. Growth of large-area 2D $MoS_{2(1-x)}Se_{2x}$ semiconductor alloys. *Adv. Mater*. **2014**, *26*, 2648–2653.
[163] Gong, Y. J.; Liu, Z.; Lupini, A. R.; Shi, G.; Lin, J. H.; Najmaei, S.; Lin, Z.; Elías, A. L.; Berkdemir, A.; You, G. et al. Band gap engineering and layer-by-layer mapping of selenium-doped molybdenum disulfide. *Nano Lett*. **2014**, *14*, 442–449.
[164] Li, H. L.; Duan, X. D.; Wu, X. P.; Zhuang, X. J.; Zhou, H.; Zhang, Q. L.; Zhu, X. L.; Hu, W.; Ren, P. Y.; Guo, P. F. et al. Growth of alloy $MoS_{2x}Se_{2(1-x)}$ nanosheets with fully tunable chemical compositions and optical properties. *J. Am. Chem. Soc*. **2014**, *136*, 3756–3759.
[165] Jing, Y.; Ma, Y. D.; Li, Y. F.; Heine, T. GeP_3: A small indirect band gap 2D crystal with high carrier mobility and strong interlayer quantum confinement. *Nano Lett*. **2017**, *17*, 1833–1838.
[166] Guan, J.; Liu, D.; Zhu, Z.; Tománek, D. Two-dimensional phosphorus carbide: Competition between sp^2 and sp^3 bonding. *Nano Lett*. **2016**, *16*, 3247–3252.
[167] Amani, M.; Regan, E.; Bullock, J.; Ahn, G. H.; Javey, A. Mid-wave infrared photoconductors based on black phosphorus-arsenic alloys. *ACS Nano* **2017**, *11*, 11724–11731.
[168] Li, L.; Wang, W. K.; Gong, P. L.; Zhu, X. D.; Deng, B.; Shi, X. Q.; Gao, G. Y.; Li, H. Q.; Zhai, T. Y. 2D GeP: An unexploited low-symmetry semiconductor with strong in-plane anisotropy. *Adv. Mater*. **2018**, *30*, 1706771.
[169] Yang, B. C.; Wan, B. S.; Zhou, Q. H.; Wang, Y.; Hu, W. T.; Lv, W. M.; Chen, Q.; Zeng, Z. M.; Wen, F. S.; Xiang, J. Y. et al. Te-doped black phosphorus field-effect transistors. *Adv. Mater*. **2016**, *28*, 9408–9415.
[170] Guo, J.; Huang, D. Z.; Zhang, Y.; Yao, H. Z.; Wang, Y. Z.; Zhang, F.; Wang, R.; Ge, Y. Q.; Song, Y. F.; Guo, Z. N. et al. 2D GeP as a novel broadband nonlinear optical material for ultrafast photonics. *Laser Photonics Rev*. **2019**, *13*, 1900123.
[171] Shirotani, I.; Mikami, J.; Adachi, T.; Katayama, Y.; Tsuji, K.; Kawamura, H.; Shimomura, O.; Nakajima, T. Phase transitions and superconductivity of black phosphorus and phosphorus-arsenic alloys at low temperatures and high pressures. *Phys. Rev. B* **1994**, *50*, 16274–16278.
[172] Barreteau, C.; Michon, B.; Besnard, C.; Giannini, E. High-pressure melt growth and transport properties of SiP, SiAs, GeP, and GeAs 2D layered semiconductors. *J. Cryst. Growth* **2016**, *443*, 75–80.
[173] Long, M. S.; Gao, A. Y.; Wang, P.; Xia, H.; Ott, C.; Pan, C.; Fu, Y. J.; Liu, E. F.; Chen, X. S.; Lu, W. et al. Room temperature high-detectivity mid-infrared photodetectors based on black arsenic phosphorus. *Sci. Adv*. **2017**, *3*, e1700589.
[174] Feng, B. J.; Zhang, J.; Zhong, Q.; Li, W. B.; Li, S.; Li, H.; Cheng, P.; Meng, S.; Chen, L.; Wu, K. H. Experimental realization of two-dimensional boron sheets. *Nat. Chem*. **2016**, *8*, 563–568.
[175] Zhang, Z. H.; Yang, Y.; Penev, E. S.; Yakobson, B. I. Elasticity, flexibility, and ideal strength of borophenes. *Adv. Funct. Mater*. **2017**, *27*, 1605059.
[176] Lherbier, A.; Botello-Méndez, A. R.; Charlier, J. C. Electronic and optical properties of pristine and oxidized borophene. *2D Mater*. **2016**, *3*, 045006.
[177] Peng, B.; Zhang, H.; Shao, H. Z.; Xu, Y. F.; Zhang, R. J.; Zhu, H. Y. The electronic, optical, and thermodynamic properties of borophene from first-principles calculations. *J. Mater. Chem. C* **2016**, *4*, 3592–3598.
[178] Zhou, H. B.; Cai, Y. Q.; Zhang, G.; Zhang, Y. W. Superior lattice thermal conductance of single-layer borophene. *npj 2D Mater. Appl*. **2017**, *1*, 14.
[179] Wang, Z. Q.; Lü, T. Y.; Wang, H. Q.; Feng, Y. P.; Zheng, J. C. High anisotropy of fully hydrogenated borophene. *Phys. Chem. Chem. Phys*. **2016**, *18*, 31424–31430.
[180] Kong, L. J.; Wu, K. H.; Chen, L. Recent progress on borophene: Growth and structures. *Front. Phys*. **2018**, *13*, 138105.
[181] Tsafack, T.; Yakobson, B. I. Thermomechanical analysis of two-dimensional boron monolayers. *Phys. Rev. B* **2016**, *93*, 165434.
[182] Wu, R. T.; Drozdov, I. K.; Eltinge, S.; Zahl, P.; Beigi, S. I.; Božović, I.; Gozar, A. Large-area single-crystal sheets of borophene on Cu(111) surfaces. *Nat. Nanotechnol*. **2019**, *14*, 44–49.
[183] Zhang, Z. H.; Penev, E. S.; Yakobson, B. I. Two-dimensional boron: Structures, properties and applications. *Chem. Soc. Rev*. **2017**, *46*, 6746–6763.
[184] Mannix, A. J.; Zhou, X. F.; Kiraly, B.; Wood, J. D.; Alducin, D.; Myers, B. D.; Liu, X. L.; Fisher, B. L.; Santiago, U.; Guest, J. R. et al. Synthesis of borophenes: Anisotropic, two-dimensional boron polymorphs. *Science* **2015**, *350*, 1513–1516.
[185] Zhang, Z. H.; Mannix, A. J.; Liu, X. L.; Hu, Z. L.; Guisinger, N. P.; Hersam, M. C.; Yakobson, B. I. Near-equilibrium growth from borophene edges on silver. *Sci. Adv*. **2019**, *5*, eaax0246.
[186] Tai, G. A.; Hu, T. S.; Zhou, Y. G.; Wang, X. F.; Kong, J. Z.; Zeng, T.; You, Y. C.; Wang, Q. Synthesis of atomically thin boron films on copper foils. *Angew. Chem., Int. Ed*. **2015**, *54*, 15473–15477.
[187] Kiraly, B.; Liu, X. L.; Wang, L. Q.; Zhang, Z. H.; Mannix, A. J.; Fisher, B. L.; Yakobson, B. I.; Hersam, M. C.; Guisinger, N. P. Borophene synthesis on Au(111). *ACS Nano* **2019**, *13*, 3816–3822.
[188] Zhang, Z. H.; Yang, Y.; Gao, G. Y.; Yakobson, B. I. Two-dimensional boron monolayers mediated by metal substrates. *Angew. Chem., Int. Ed*. **2015**, *54*, 13022–13026.
[189] Ji, X. Y.; Kong, N.; Wang, J. Q.; Li, W. L.; Xiao, Y. L.; Gan, S. T.; Zhang, Y.; Li, Y. J.; Song, X. R.; Xiong, Q. Q. et al. A novel top-down synthesis of ultrathin 2D boron nanosheets for multimodal imaging-guided cancer therapy. *Adv. Mater*. **2018**, *30*, 1803031.
[190] Ma, D. T.; Wang, R.; Zhao, J. L.; Chen, Q. Y.; Wu, L. M.; Li, D. L.; Su, L. M.; Jiang, X. T.; Luo Z.; Ge, Y. Q. et al. A self-powered photodetector based on two-dimensional boron nanosheets. *Nanoscale* **2020**, *12*, 5313–5323.
[191] Ma, D. T.; Zhao, J. L.; Xie, J. L.; Zhang, F.; Wang, R.; Wu, L. M.; Liang, W. Y.; Li, D. L.; Ge, Y. Q.; Li, J. Q. et al. Ultrathin boron nanosheets as an emerging two-dimensional photoluminescence material for bioimaging. *Nanoscale Horiz*. **2020**, *5*, 705–713.
[192] Wang, Y. J.; Fan, J. F.; Trenary, M. Surface chemistry of boron oxidation. 1. reactions of oxygen and water with boron films grown on Tantalum(110). *Chem. Mater*. **1993**, *5*, 192–198.
[193] Cui, Z. H.; Jimenez-Izal, E. J.; Alexandrova, A. N. Prediction of two-dimensional phase of boron with anisotropic electric conductivity. *J. Phys. Chem. Lett*. **2017**, *8*, 1224–1228.
[194] Liu, F. C.; Zheng, S. J.; He, X. X.; Chaturvedi, A.; He, J. F.; Chow, W. L.; Mion, T. R.; Wang, X. L.; Zhou, J. D.; Fu Q. D. et al. Highly sensitive detection of polarized light using anisotropic 2D ReS_2. *Adv. Funct. Mater*. **2016**, *26*, 1169–1177.
[195] Zhang, E. Z.; Wang, P.; Li, Z.; Wang, H. F.; Song, C. Y.; Huang, C.; Chen, Z. G.; Yang, L.; Zhang, K. T.; Lu, S. H. et al. Tunable ambipolar polarization-sensitive photodetectors based on high-anisotropy $ReSe_2$ nanosheets. *ACS Nano* **2016**, *10*, 8067–8077.
[196] Qin, G. Z.; Qin, Z. Z.; Fang, W. Z.; Zhang, L. C.; Yue, S. Y.; Yan, Q. B.; Hu, M.; Su, G. Diverse anisotropy of phonon transport in two-dimensional group IV-VI compounds: A comparative study. *Nanoscale* **2016**, *8*, 11306–11319.
[197] Gomes, L. C.; Carvalho, A.; Neto, A. H. C. Enhanced piezoelectricity and modified dielectric screening of two-dimensional group-IV monochalcogenides. *Phys. Rev. B* **2015**, *92*, 214103.
[198] Guo, Y.; Zhou, S.; Bai, Y. Z.; Zhao, J. J. Oxidation resistance of monolayer group-IV monochalcogenides. *ACS Appl. Mater. Interfaces* **2017**, *9*, 12013–12020.
[199] Kamal, C.; Chakrabarti, A.; Ezawa, M. Direct band gaps in group IV-VI monolayer materials: Binary counterparts of phosphorene. *Phys. Rev. B* **2016**, *93*, 125428.
[200] Ryder, C. R.; Wood, J. D.; Wells, S. A.; Yang, Y.; Jariwala, D.; Marks, T. J.; Schatz, G. C.; Hersam, M. C. Covalent functionalization and

passivation of exfoliated black phosphorus via aryl diazonium chemistry. *Nat. Chem.* **2016**, *8*, 597–602.
[201] Hofmann, W. Ergebnisse der strukturbestimmung komplexer sulfide. *Z. Krist-Cryst. Mater.* **1935**, *92*, 161–185.
[202] Okazaki, A.; Ueda, I. The crystal structure of stannous selenide SnSe. *J. Phys. Soc. Jpn.* **1956**, *11*, 470.
[203] Okazaki, A. The crystal structure of germanium selenide GeSe. *J. Phys. Soc. Jpn.* **1958**, *13*, 1151–1155.
[204] Brent, J. R.; Lewis, D. J.; Lorenz, T.; Lewis, E. A.; Savjani, N.; Haigh, S. J.; Seifert, G.; Derby, B.; O'Brien, P. Tin(II) sulfide (SnS) nanosheets by liquid-phase exfoliation of herzenbergite: IV-VI main group two-dimensional atomic crystals. *J. Am. Chem. Soc.* **2015**, *137*, 12689–12696.
[205] Ramasamy, K.; Kuznetsov, V. L.; Gopal, K.; Malik, M. A.; Raftery, J.; Edwards, P. P.; O'Brien, P. Correction to organotin dithiocarbamates: Single-source precursors for tin sulfide thin films by aerosol-assisted chemical vapor deposition (AACVD). *Chem. Mater.* **2014**, *25*, 3348.
[206] Gomes, L. C.; Carvalho, A.; Neto, A. H. C. Vacancies and oxidation of two-dimensional group-IV monochalcogenides. *Phys. Rev. B* **2016**, *94*, 054103.
[207] Santosh, K. C.; Longo, R. C.; Wallace, R. M.; Cho, K. Surface oxidation energetics and kinetics on MoS_2 monolayer. *J. Appl. Phys.* **2015**, *117*, 135301.
[208] Zhang, T. M.; Wan, Y. Y.; Xie, H. Y.; Mu, Y.; Du, P. W.; Wang, D.; Wu, X. J.; Ji, H. X.; Wan, L. J. Degradation chemistry and stabilization of exfoliated few-layer black phosphorus in water. *J. Am. Chem. Soc.* **2018**, *140*, 7561–7567.
[209] Venuthurumilli, P. K.; Ye, P. D.; Xu, X. F. Plasmonic resonance enhanced polarization-sensitive photodetection by black phosphorus in near infrared. *ACS Nano* **2018**, *12*, 4861–4867.
[210] Zhou, W. H.; Zhang, S. L.; Wang, Y. Y.; Guo, S. Y.; Qu, H. Z.; Bai, P. X.; Li, Z.; Zeng, H. B. Anisotropic in-plane ballistic transport in monolayer black arsenic‐phosphorus FETs. *Adv. Electron. Mater.* **2020**, *6*, 1901281.
[211] Zhong, M. Z.; Xia, Q. L.; Pan, L. F.; Liu, Y. Q.; Chen, Y. B.; Deng, H. X.; Li, J. B.; Wei, Z. M. Thickness-dependent carrier transport characteristics of a new 2D elemental semiconductor: Black arsenic. *Adv. Funct. Mater.* **2018**, *28*, 1802581.
[212] Mahmoud, M. M. A.; Joubert, D. P. First principles study of the structural, stability properties and lattice thermal conductivity of bulk $ReSe_2$. *Mater. Today Proc.* **2018**, *5*, 10424–10430.
[213] Wu, J. B.; Zhao, H.; Li, Y. R.; Ohlberg, D.; Shi, W.; Wu, W.; Wang, H.; Tan, P. H. Monolayer molybdenum disulfide nanoribbons with high optical anisotropy. *Adv. Opt. Mater.* **2016**, *4*, 756–762.
[214] Liu, S. J.; Xiao, W. B.; Zhong, M. Z.; Pan, L. F.; Wang, X. T.; Deng, H. X.; Liu, J.; Li, J. B.; Wei, Z. M. Highly polarization sensitive photodetectors based on quasi-1D titanium trisulfide (TiS_3). *Nanotechnology* **2018**, *29*, 184002.
[215] Niu, S. Y.; Joe, G.; Zhao, H.; Zhou, Y. C.; Orvis, T.; Huyan, H. X.; Salman, J.; Mahalingam, K.; Urwin, B.; Wu, J. B. et al. Giant optical anisotropy in a quasi-one-dimensional crystal. *Nat. Photonics* **2018**, *12*, 392–396.
[216] Ma, Y. Q.; Shen, C. F.; Zhang, A. Y.; Chen, L.; Liu, Y. H.; Chen, J. H.; Liu, Q. Z.; Li, Z.; Amer, M. R.; Nilges, T. et al. Black phosphorus field-effect transistors with work function tunable contacts. *ACS Nano* **2017**, *11*, 7126–7133.
[217] Chen, Y. T.; Ren, R.; Pu, H. H.; Chang, J. B.; Mao, S.; Chen, J. H. Field-effect transistor biosensors with two-dimensional black phosphorus nanosheets. *Biosens. Bioelectron.* **2017**, *89*, 505–510.
[218] Wu, L. M.; Dong, Y. Z.; Zhao, J. L.; Ma, D. T.; Huang, W. C.; Zhang, Y.; Wang, Y. Z.; Jiang, X. T.; Xiang, Y. J.; Li, J. Q. et al. Kerr nonlinearity in 2D graphdiyne for passive photonic diodes. *Adv. Mater.* **2019**, *31*, 1807981.
[219] Ren, X. H.; Li, Z. J.; Huang, Z. Y.; Sang, D.; Qiao, H.; Qi, X.; Li, J. Q.; Zhong, J. X.; Zhang, H. Environmentally robust black phosphorus nanosheets in solution: Application for self-powered photodetector. *Adv. Funct. Mater.* **2017**, *27*, 1606834.
[220] Hao, C. X.; Yang, B. C.; Wen, F. S.; Xiang, J. Y.; Li, L.; Wang, W. H.; Zeng, Z. M.; Xu, B.; Zhao, Z. S.; Liu, Z. Y. et al. Flexible all-solid-state supercapacitors based on liquid-exfoliated black-phosphorus nanoflakes. *Adv. Mater.* **2016**, *28*, 3194–3201.